GSA Data Repository item 2019160

Long, S.P., Mullady, C.L., Starnes, J.K., Gordon, S.M., Larson, K.P., Pianowski, L.S., Miller, R.B., and Soignard, E., A structural model for the South Tibetan detachment system in northwestern Bhutan from integration of temperature, fabric, strain, and kinematic data: Lithosphere, v. 11, https://doi.org/10.1130/L1049.1

Table DR1 (following 2 pages): Details on thin sections from the Dodena-Lingshi transect, listed from structurally-low to high.

Thin section number in text	Original thin section number	Latitude (dd.ddddd)	Longitude (dd.ddddd)	Altitude (m)	Structural height relative to base of Chekha Fm (m)	Map unit	Lithology	Foliation (d, dd)[1]	Lineation (tr, pl)[2]	Crenulation cleavage axis (tr, pl)[2]	Orientation relative to lineation	Thin section orientation (d, dd)[1]	Major mineral phases[3]	Quartz recrystallization mechanism[4]	Shear-sense indicators
33	LP-33A	27.85516	89.43079	4200	9675	THMzu	slate	11, 225	-	12, 020	normal to crenulation	84, 222	clay minerals,gr,qz	not recrystallized	none
	LP-33B										parallel to crenulation	85, 112			
34	LP-34A	27.86438	89.44403	4040	9575	THMzu	graphitic slate	38, 355	21, 300	-	parallel to lineation	57, 220	gr,clay minerals,qz	not recrystallized	none
	LP-34B										normal to lineation	67, 121			
35	LP-35A	27.85412	89.43924	4000	9475	THMzu	graphitic slate	7, 324	13, 338	-	parallel to lineation	89, 248	gr,clay minerals,qz	not recrystallized	none
	LP-35B										normal to lineation	87, 160			
36	LP-36A	27.82490	89.43178	4100	8775	THMzu	graphitic slate	19, 155	9, 201	-	parallel to lineation	74, 298	gr,clay minerals,qz	not recrystallized	none
	LP-36B										normal to lineation	77, 021			
37	LP-37A	27.81483	89.43172	4200	8450	THMzu	graphitic slate	75, 352	64, 298	-	parallel to lineation	69, 259	gr,clay minerals,qz	not recrystallized	none
	LP-37B										normal to lineation	27, 127			
42	LP-42	27.76037	89.45203	4760	6750	THPzu	graphitic slate	35, 050	11, 348	-	parallel to lineation	57, 254	clay minerals,gr,qz	not recrystallized	none
43	LP-43	27.75631	89.45795	4680	6650	THPzu	slate	30, 000	30, 354	-	parallel to lineation	86, 266	clay minerals,qz	not recrystallized	top-N SC fabric, top-S asymmetric fold
44	LP-44	27.74113	89.45821	4400	5850	THPzu	limestone	34, 205	11, 132	-	parallel to lineation	59, 049	cal,gr,clay minerals	not recrystallized	none
45	LP-45A	27.72113	89.45913	4240	5700	THPzu	quartzite	16, 322	16, 316	-	parallel to lineation	87, 227	qz,clay minerals	not recrystallized	none
	LP-45B										normal to lineation	74, 147			
46	LP-46A	27.71117	89.47379	3960	4950	THCk	marble	40, 350	40, 342	-	parallel to lineation	86, 256	cal,qz,clay minerals	not recrystallized	none
	LP-46B										normal to lineation	51, 164			
48	LP-48A	27.71112	89.48012	3960	4700	THCk	marble	25, 325	22, 293	-	parallel to lineation	82, 209	cal,qz	not recrystallized	top-SE C'-type shear bands
	LP-48B										normal to lineation	69, 114			
49	LP-49A	27.71088	89.48080	3960	4650	THCk	marble	44, 356	16, 315	-	parallel to lineation	61, 233	cal,clay minerals,qz,gr,ms	not recrystallized	none
	LP-49B										normal to lineation	56, 136			
50	LP-50A	27.71180	89.48540	3920	4425	THCk	phyllite	5, 050	1, 334	5, 043	parallel to lineation	86, 243	cal,clay minerals,qz,gr	not recrystallized	top-SE SC fabric
	LP-50B										normal to lineation	90, 152			
51	LP-51	27.71247	89.50758	3800	3675	THCk	marble	16, 005	-	-	parallel to lineation	not oriented	cal	no qz	none
52	LP-52A	27.71179	89.51206	3800	3600	THCk	marble	21, 355	14, 309	-	parallel to lineation	73, 221	cal,qz,clay minerals,ms,gr	not recrystallized	none
	LP-52B										normal to lineation	76, 130			
53	LP-53A	27.70963	89.52175	3800	3275	THCk	marble	41, 334	41, 292	-	parallel to lineation	66, 216	cal,qz,oxides,clay minerals	not recrystallized	none
	LP-53B										normal to lineation	58, 111			
54	LP-54	27.70990	89.52418	3760	3255	THCk	marble	20, 306	-	-	normal to crenulation	not oriented	cal,qz,ms	not recrystallized	none
103	SB16-103	27.70792	89.54231	3660	2700	THCk	marble	51, 200	-	27, 566	normal to crenulation	50, 068	cal,ms,clay minerals,qz	BLG	none
101	SB16-101A	27.70011	89.55153	3640	2375	THCk	calcareous phyllite	20, 290	0, 020	19, 260	parallel to lineation	71, 110	cal,ms,qz,gr	not recrystallized	top-SW crenulated SC fabric
	SB16-101B										normal to lineation	88, 200			
99	SB16-99A	27.69469	89.56486	3590	2225	THCk	marble	9, 265	2, 335	-	parallel to lineation	82, 064	cal,ms,clay minerals	not recrystallized	none
	SB16-99B										normal to lineation	87, 157			
97	SB16-97A	27.69264	89.57447	3580	1975	THCk	phyllitic quartzite	22, 235	17, 192	-	parallel to lineation	76, 108	qz,ms,clay minerals	SGR	top-S crenulated SC fabric
	SB16-97B										normal to lineation	74, 011			
95	SB16-95A	27.69189	89.58142	3610	1775	THCk	marble	12, 230	-	12, 246	normal to crenulation	88, 065	cal,qz,ms,clay minerals	SGR	none
	SB16-95B										parallel to crenulation	87, 335			
93	SB16-93A	27.69431	89.59094	3750	1600	THCk	marble	26, 275	26, 281	-	parallel to lineation	89, 010	cal,ms,qz	SGR	none
	SB16-93B										normal to lineation	64, 103			
105	SB16-105A	27.68431	89.60744	3610	1275	THCk	marble	25, 240	17, 007	-	parallel to lineation	71, 103	cal,qz,bt	not recrystallized	none
	SB16-105B										normal to lineation	76, 006			
108	SB16-108A	27.68022	89.61319	3425	1175	THCk	marble	16, 165	-	2, 084	normal to crenulation	85, 265	cal,qz,ms	not recrystallized	none
	SB16-108B										parallel to crenulation	75, 354			
110	SB16-110A	27.67953	89.62058	3370	850	THCk	marble	10, 310	7, 281	-	parallel to lineation	85, 194	cal,calc-silicates,qz	SGR	none
	SB16-110B										normal to lineation	82, 101			
91	SB16-91A	27.67858	89.64061	3380	775	THCk	schist	10, 220	5, 155	6, 277	parallel to lineation	81, 065	qz,bt,chl	SGR	top-NW mica fish
	SB16-91B										normal to lineation	87, 345			
111	SB16-111	27.68111	89.62297	3385	750	THCk	granite	-	-	-	random (no lineation)	not oriented	kfs,qz,pl,ms,bt	SGR	none
89	SB16-89A	27.66994	89.64222	3820	700	THCk	calcareous quartzite	14, 250	10, 172	-	parallel to lineation	76, 084	qz,bt,cal,calc-silicates,pl	SGR	none
	SB16-89B										normal to lineation	87, 351			
88	SB16-88	27.66800	89.63953	3280	575	THCk	calc-sili gneiss	21, 300	20, 356	-	parallel to lineation	83, 082	qz,calc-silicates,cal	SGR	none
113	SB16-113A	27.68083	89.63486	3380	450	THCk	calc-silicate gneiss	16, 215	8, 153	-	parallel to lineation	76, 064	qz,calc-silicates,bt,cal	SGR	none
	SB16-113B										normal to lineation	83, 333			
87	SB16-87	27.66678	89.63936	3285	425	THCk	granite	-	-	-	random (no lineation)	not oriented	kfs,qz,pl,tur,ms	SGR	none
84	SB16-84A	27.65675	89.64372	3505	250	THCk	schist	11, 215	10, 184	-	parallel to lineation	84, 095	qz,bt,pl,gr	SGR	none
	SB16-84B										normal to lineation	81, 005			
83	SB16-83A	27.65253	89.64397	3505	175	THCk	schist	17, 340	17, 345	-	parallel to lineation	89, 255	qz,bt,gr,calc-silicates	SGR	none
	SB16-83B										normal to lineation	73, 168			
82	SB16-82	27.64994	89.64233	3475	150	THCk	quartzite	17, 275	14, 316	-	parallel to lineation	81, 043	qz,ms,bt,calc-silicates,pl	SGR	top-NW SC fabric
21C	SB16-21C	27.63250	89.62972	3345	0	GH	calc-silicate gneiss	-	-	-	random	not oriented	calc-silicates,pl,cal,qz,kfs	not recrystallized	none
21B	SB16-21B	27.63250	89.62972	3345	0	GH	granite	-	-	-	parallel to lineation	not oriented	kfs,qz,pl,bt,ms	SGR	none

21A	SB16-21A	27.63250	89.62972	3345	0	GH	quartzite	14, 290	11, 336	-	parallel to lineation	82, 063	qz,ms,pl	SGR	top-NW qz oblique SPO, mica fish
20	SB16-20	27.62897	89.63172	3300	-25	GH	schist	14, 045	10, 089	-	parallel to lineation	82, 180	bt,qz,kfs,sil,grt,pl,ms	GBM	top-NW qz sigma objects
17B	SB16-17B	27.62042	89.63331	3180	-475	GH	granite	-	-	-	random (no lineation)	not oriented	kfs,qz,pl,ms,bt	not recrystallized	none
17A	SB16-17A	27.62042	89.63331	3180	-475	GH	orthogneiss	16, 200	16, 194	-	parallel to lineation	89, 106	kfs,qz,pl,bt,ms	GBM	top-S C'-type shear band
14	SB16-14	27.61553	89.63619	3285	-650	GH	quartzite	23, 340	18, 303	-	parallel to lineation	74, 217	qz,kfs,bt,ms	GBM	top-NW qz oblique SPO
13	SB16-13	27.61375	89.63575	3240	-700	GH	quartzite	28, 340	26, 318	-	parallel to lineation	78, 233	qz,grt,pl,bt,chl,cal	SGR	none
12	SB16-12	27.61297	89.63697	3215	-800	GH	calc-silicate gneiss	11, 020	-	-	along 325° azimuth	83, 254	qtz,calc-silicates,cal,pl,bt	SGR	none
11	SB16-11	27.60992	89.63606	3100	-925	GH	granite	-	-	-	parallel to lineation	not oriented	kfs,qz,pl,ms,bt	GBM	none
10	SB16-10	27.60939	89.63561	3065	-1025	GH	quartzite	31, 355	30, 348	-	parallel to lineation	85, 261	qz,bt,pl	SGR overprints GBM	top-N qz oblique SPO
9	SB16-9	27.61114	89.63347	3000	-1075	GH	schist	-	-	-	parallel to lineation	not oriented	qz,bt,sil,kfs,ms,grt	GBM	none
7	SB16-7	27.60739	89.63114	2835	-1325	GH	quartzite	21, 000	19, 344	-	parallel to lineation	82, 258	qz,bt,pl,ms	CBE	none
6	SB16-6	27.60550	89.63419	2775	-1400	GH	paragneiss	30, 355	29, 337	-	parallel to lineation	81, 251	qz,bt,sil,ms,grt	GBM	none
3	SB16-3	27.59936	89.63108	2630	-1550	GH	quartzite	24, 320	24, 320	-	parallel to lineation	90, 230	qz,bt,sil,ms,kfs	CBE	top-NW SC fabric
1	SB16-1	27.59542	89.63061	2595	-1825	GH	siliceous paragneiss	17, 355	16, 004	-	parallel to lineation	89, 275	qz,ms,bt,sil,grt	GBM	top-N mica fish, qz sigma object
26	SB16-26	27.57564	89.63747	2535	-2950	GH	paragneiss	35, 000	20, 306	-	parallel to lineation	59, 227	qz,bt,pl,kfs,ms,grt,sil	CBE	none
28	SB16-28	27.55689	89.64758	2550	-3850	GH	paragneiss	21, 300	16, 342	-	parallel to lineation	77, 068	qz,bt,sil,ms,kfs	CBE	top-NW qz sigma clasts
30	SB16-30	27.54972	89.65136	2570	-3950	GH	paragneiss	30, 260	4, 178	-	parallel to lineation	60, 272	qz,bt,pl,kfs,sil,ms,grt	CBE	top-S qz sigma clasts

[1](d, dd) stands for dip, dip direction notation. [2](tr, pl) stands for trend, plunge notation. [3]Mineral abbreviations after Whitney and Evans (2010).

[4]BLG = bulging recrystallization, SGR = subgrain rotation, GBM = grain boundary migration without chessboard extinction, CBE = grain boundary migration with chessboard extinction.

Discussion DR1: Analytical methods and supporting data for RSCM thermometry

Measurements were made at the LeRoy Eyring Center for Solid State Science at Arizona State University, using a Raman spectrometer custom-built by E. Soignard. Carbonaceous material (CM) was analyzed *in situ* on polished, foliation-normal, lineation-parallel thin sections. The 532 nm laser was focused using a 50x ultra-long working distance Mitutoyo objective and attenuated to a power of 3 mW at the sample. The probed area of CM for each measurement was approximately 1 μm in diameter. Instrument parameters, settings, and procedures followed those outlined in Cooper et al. (2013) and Long et al. (2016; 2017). The laser was focused on CM situated beneath a transparent grain (typically quartz or calcite), after procedures outlined in Beyssac et al. (2003). CM was analyzed for 120 seconds over a spectral window of 1100-2000 cm^{-1}. Multiple grains of CM were analyzed from each sample (the total range is between 9 and 16 grains per sample), to allow evaluation of in-sample variation.

The center positions, heights, widths, and areas of four first-order Raman peaks, including the G peak and three defect bands, D1, D2, and D3, are shown for individual analyses on Table DR2. These parameters were determined using a peak fitting program written in Matlab by E. Soignard, which allowed peaks to be fit by a combination of Gaussian and Lorentzian peak shape, and background slope to be removed by using a 1^{st}-order polynomial. R1 and R2 correspond to the height and area ratios as defined in equations 1 and 2 of Rahl et al. (2005), and the peak temperature (T_{peak}) for each analysis is calculated from equation 3 of Rahl et al. (2005). Analyses of each sample on Table DR2 are ordered from low to high peak temperature. Standard means of R1, R2, and T_{peak} for all analyses from each sample are shown. The internal variation of R1, R2, and T_{peak} from each sample is represented by 1 standard deviation on the mean. However, the calibration equation of Rahl et al. (2005) also introduces an external ± 50 °C uncertainty in T_{peak}. Therefore, after Cooper et al. (2013), in order to present a more representative uncertainty, we calculated a propagated standard error (SE) by adding internal and external uncertainties quadratically, and dividing by the square root of the number of analyses (n). Mean T_{peak} with this propagated 2 SE uncertainty is reported for each sample on Table 1 in the text. At 2 SE, typical error ranges are ± 30-50 °C.

Table DR2 (following 6 pages): Supporting data for RSCM T_{peak} determinations. Data for individual CM spot analyses for each sample are shown, and are ordered from low to high T_{peak}. Refer to Table DR1 for a guide to abbreviated sample numbers used in the text.

Sample and	Peak center position				Peak width				Peak amplitude				Peak area				Ratios		T_{peak}
spot number	D1	D3	G	D2	D1	D3	G	D2	D1	D3	G	D2	D1	D3	G	D2	R1	R2	(°C)
SB16-30_spot3	1363	1550	1587	1623	37	70	15	21	100	0	1530	45	5437	0	36050	1005	0.065	0.128	621
SB16-30_spot10	1361	1550	1586	1623	31	70	16	14	155	0	2200	30	6816	0	51834	447	0.071	0.115	637
SB16-30_spot1	1363	1550	1586	1621	32	70	16	18	95	0	1905	35	4467	0	44785	670	0.050	0.090	658
SB16-30_spot13	1362	1550	1587	1621	35	70	15	21	62	0	1730	25	3078	0	40762	558	0.036	0.069	675
SB16-30_spot6	1364	1550	1586	1615	36	70	16	17	25	0	910	29	1414	0	21024	524	0.028	0.062	680
SB16-30_spot2	1360	1550	1586	1619	40	70	16	22	31	0	1790	25	1948	0	42082	585	0.017	0.044	696
SB16-30_spot7	1363	1550	1587	1617	31	70	16	15	20	0	1080	25	974	0	25390	399	0.019	0.036	704
SB16-30_spot5	1365	1550	1586	1619	45	70	16	19	14	0	1255	33	990	0	29569	667	0.011	0.032	706
SB16-30_spot12	1365	1550	1587	1619	30	70	15	19	18	0	1070	40	821	0	24397	808	0.017	0.032	709
SB16-30_spot9	1360	1550	1586	1619	32	70	16	16	10	0	1360	22	421	0	31973	374	0.007	0.013	726
SB16-30_spot16	1365	1550	1587	1620	25	70	15	18	11	0	1620	15	362	0	36938	287	0.007	0.010	729
SB16-30_spot18	1363	1550	1586	1619	25	70	15	18	8	0	1695	16	289	0	38648	306	0.005	0.007	731
SB16-30_spot11	1362	1550	1587	1620	35	70	15	12	5	0	2020	15	257	0	47595	191	0.002	0.005	732
SB16-30_spot17	1366	1550	1586	1621	20	70	15	15	11	0	2030	10	290	0	46286	160	0.005	0.006	732
SB16-30_spot15	1363	1550	1586	1618	31	70	15	15	1	0	1595	20	41	0	35761	319	0.001	0.001	736
																mean:	0.023	0.043	698
																1σ (internal):	0.023	0.040	36
																1 SE (internal):	0.006	0.010	9
																propagated 2 SE (internal and external):			32
																n:			15
SB16-3_spot14	1363	1550	1586	1621	35	70	16	22	22	0	175	31	1092	0	4256	725	0.126	0.180	584
SB16-3_spot5	1365	1550	1586	1623	37	70	16	24	57	0	595	8	2588	0	14019	204	0.096	0.154	603
SB16-3_spot2	1364	1550	1585	1619	38	70	16	21	19	0	298	22	1134	0	7006	491	0.064	0.131	618
SB16-3_spot16	1361	1550	1585	1623	32	70	15	20	63	0	520	40	2246	0	12252	851	0.121	0.146	619
SB16-3_spot15	1363	1550	1585	1620	35	70	14	17	14	0	240	10	645	0	5278	181	0.058	0.106	643
SB16-3_spot13	1365	1550	1585	1615	50	70	16	17	6	0	183	40	410	0	4599	723	0.033	0.072	671
SB16-3_spot3	1362	1550	1585	1621	40	70	15	18	11	0	840	6	691	0	19153	115	0.013	0.035	705
SB16-3_spot6	1366	1550	1587	1617	32	70	15	18	12	0	705	115	564	0	16611	2201	0.017	0.029	712
SB16-3_spot4	1365	1550	1585	1622	30	70	16	15	3	0	740	12	141	0	17397	191	0.004	0.008	730
																mean:	0.059	0.096	654
																1σ (internal):	0.044	0.059	50
																1 SE (internal):	0.015	0.020	17
																propagated 2 SE (internal and external):			47
																n:			9
SB16-9_spot6	1358	1550	1585	1617	31	70	15	18	47	0	825	65	2215	0	18183	1244	0.057	0.102	646
SB16-9_spot12	1362	1550	1586	1619	42	70	16	17	31	0	670	100	2045	0	16839	1808	0.046	0.099	647
SB16-9_spot14	1361	1550	1586	1622	35	70	15	17	43	0	850	50	2059	0	18087	904	0.051	0.098	649
SB16-9_spot8	1365	1550	1586	1618	40	70	15	20	27	0	1080	5	1587	0	23804	106	0.025	0.063	679
SB16-9_spot5	1360	1550	1585	1620	35	70	15	15	29	0	1170	25	1594	0	26677	399	0.025	0.056	686
SB16-9_spot4	1358	1550	1584	1622	38	70	15	16	35	0	1630	55	1954	0	38406	936	0.022	0.047	694
SB16-9_spot9	1362	1550	1585	1620	31	70	15	12	23	0	1050	10	1120	0	22371	128	0.022	0.047	694
SB16-9_spot1	1354	1550	1585	1621	38	70	15	12	26	0	1460	20	1552	0	32178	255	0.018	0.046	694
SB16-9_spot10	1366	1550	1585	1620	30	70	15	15	17	0	1420	15	801	0	30254	239	0.012	0.026	714
SB16-9_spot13	1355	1550	1586	1622	44	70	15	11	9	0	1520	20	622	0	34657	234	0.006	0.018	721
SB16-9_spot3	1358	1550	1585	1624	34	70	15	10	10	0	1580	5	465	0	36026	53	0.006	0.013	726
SB16-9_spot17	1362	1550	1586	1622	30	70	15	12	7	0	1330	1	255	0	31337	13	0.005	0.008	730
SB16-9_spot18	1365	1550	1586	1620	25	70	16	14	3	0	1240	1	91	0	30158	15	0.002	0.003	735
SB16-9_spot16	1355	1550	1586	1625	40	70	15	16	1	0	1430	1	49	0	32605	17	0.001	0.001	736
																mean:	0.021	0.045	696
																1σ (internal):	0.018	0.034	31
																1 SE (internal):	0.005	0.009	8
																propagated 2 SE (internal and external):			31
																n:			14
SB16-20_spot4	1350	1550	1584	1621	40	70	16	21	145	0	1650	70	7345	0	38790	1563	0.088	0.154	601
SB16-20_spot18	1364	1550	1585	1619	38	70	16	21	19	0	298	22	1134	0	7006	491	0.078	0.135	618
SB16-20_spot6	1348	1550	1583	1621	39	70	19	17	205	0	2020	100	9719	0	58340	1808	0.101	0.139	621
SB16-20_spot5	1351	1550	1584	1623	42	70	16	15	168	0	2320	80	8578	0	56425	1276	0.072	0.129	622
SB16-20_spot7	1347	1550	1583	1622	40	70	19	19	124	0	1550	35	6785	0	44766	707	0.080	0.130	624
SB16-20_spot1	1347	1550	1584	1622	46	70	16	15	127	0	2270	80	7991	0	57051	1276	0.056	0.120	627
SB16-20_spot14	1350	1550	1585	1619	41	70	19	18	95	0	1080	130	4933	0	30671	2489	0.088	0.129	627
SB16-20_spot12	1352	1550	1585	1624	38	70	19	15	71	0	1110	28	3691	0	30988	447	0.064	0.105	645
SB16-20_spot9	1352	1550	1584	1622	45	70	19	17	62	0	1200	42	3958	0	34657	759	0.052	0.101	646
SB16-20_spot11	1343	1550	1585	1621	48	70	19	17	50	0	1360	130	3648	0	38623	2350	0.037	0.082	662
SB16-20_spot10	1353	1550	1585	1621	43	70	19	20	59	0	1300	50	3470	0	37546	1063	0.045	0.083	664
SB16-20_spot3	1347	1550	1584	1622	44	70	16	15	70	0	2050	80	4526	0	51522	1276	0.034	0.079	664
SB16-20_spot16	1353	1550	1586	1625	41	70	17	14	1	0	920	8	52	0	22980	119	0.001	0.002	735
SB16-20_spot15	1353	1550	1585	1619	41	70	17	18	1	0	1500	1	52	0	37468	19	0.001	0.001	736
																mean:	0.057	0.099	649
																1σ (internal):	0.030	0.046	40
																1 SE (internal):	0.008	0.012	11
																propagated 2 SE (internal and external):			34
																n:			14
SB16-83_spot11	1356	1550	1584	1618	39	70	15	22	65	0	430	45	3210	0	9478	1053	0.151	0.234	534

SB16-83_spot14	1349	1550	1583	1617	38	70	22	18	145	0	900	100	7537	0	28088	1914	0.161	0.201	572
SB16-83_spot15	1351	1550	1583	1615	36	70	22	20	160	0	870	170	7587	0	26666	3616	0.184	0.200	580
SB16-83_spot12	1357	1550	1585	1620	37	70	15	18	110	0	1100	25	5154	0	25081	479	0.100	0.168	589
SB16-83_spot7	1355	1550	1584	1616	43	70	15	18	23	0	750	25	1554	0	15979	479	0.031	0.086	655
SB16-83_spot1	1351	1550	1582	1623	30	70	20	12	150	0	1970	40	6612	0	61889	510	0.076	0.096	659
SB16-83_spot13	1355	1550	1582	1620	35	70	16	11	70	0	1450	20	3103	0	35265	234	0.048	0.080	667
SB16-83_spot4	1349	1550	1583	1620	29	70	17	10	70	0	1650	1	3086	0	41384	11	0.042	0.069	677
SB16-83_spot5	1344	1550	1583	1620	41	70	17	10	13	0	640	1	837	0	14713	11	0.020	0.054	686
SB16-83_spot6	1346	1550	1583	1614	41	70	16	8	15	0	970	10	966	0	22017	85	0.016	0.042	698
SB16-83_spot17	1356	1550	1581	1620	35	70	19	15	12	0	820	8	596	0	23829	128	0.015	0.024	716
SB16-83_spot3	1348	1550	1581	1620	30	70	16	10	20	0	1750	5	942	0	42562	53	0.011	0.022	718
SB16-83_spot16	1352	1550	1582	1624	30	70	20	12	13	0	850	17	514	0	24354	217	0.015	0.021	720
																mean:	0.067	0.100	652
																1σ (internal):	0.060	0.072	60
																1 SE (internal):	0.017	0.020	17
																		propagated 2 SE (internal and external):	43
																		n:	13
SB16-84_spot18	1353	1550	1585	1621	47	70	17	12	61	0	780	20	4503	0	20156	255	0.078	0.181	569
SB16-84_spot12	1350	1550	1585	1618	45	70	19	15	42	0	455	10	2777	0	13141	160	0.092	0.173	582
SB16-84_spot10	1356	1550	1585	1627	42	70	19	12	125	0	1460	30	7448	0	40372	383	0.086	0.155	599
SB16-84_spot9	1355	1550	1584	1625	44	70	19	14	105	0	1380	18	6554	0	38160	268	0.076	0.146	605
SB16-84_spot8	1354	1550	1584	1627	40	70	18	11	110	0	1380	15	5795	0	37758	175	0.080	0.133	620
SB16-84_spot2	1356	1550	1584	1619	34	70	15	13	50	0	830	20	2325	0	17030	277	0.060	0.118	630
SB16-84_spot4	1356	1550	1585	1623	35	70	17	10	65	0	1000	1	3112	0	24547	11	0.065	0.113	637
SB16-84_spot3	1357	1550	1584	1623	38	70	17	10	90	0	1670	5	4505	0	40274	53	0.054	0.100	648
SB16-84_spot5	1340	1550	1585	1616	55	70	16	15	12	0	530	14	903	0	11862	223	0.023	0.070	670
SB16-84_spot7	1355	1550	1585	1618	30	70	16	12	35	0	890	0	1330	0	20201	0	0.039	0.062	684
SB16-84_spot16	1353	1550	1584	1628	45	70	15	12	17	0	970	0	1202	0	20641	0	0.018	0.055	684
SB16-84_spot6	1380	1550	1585	1618	20	70	16	12	10	0	2150	1	274	0	48120	13	0.005	0.006	733
																mean:	0.056	0.109	638
																1σ (internal):	0.028	0.051	46
																1 SE (internal):	0.008	0.015	13
																		propagated 2 SE (internal and external):	39
																		n:	12
SB16-113_spot7	1354	1550	1588	1629	53	70	28	22	105	0	310	25	7895	0	12313	585	0.339	0.380	431
SB16-113_spot15	1359	1550	1592	1628	45	70	29	16	400	0	820	120	24622	0	34941	2042	0.488	0.413	434
SB16-113_spot9	1351	1550	1588	1623	51	70	27	22	90	0	220	20	6279	0	9331	468	0.409	0.391	438
SB16-113_spot10	1359	1550	1591	1627	48	70	30	19	880	0	1700	220	55636	0	74936	4445	0.518	0.412	442
SB16-113_spot17	1359	1550	1592	1629	45	70	25	16	1200	0	2950	360	73865	0	112105	6126	0.407	0.385	444
SB16-113_spot6	1354	1550	1588	1629	40	70	20	14	635	0	1970	120	32167	0	57892	1787	0.322	0.350	459
SB16-113_spot4	1354	1550	1588	1629	43	70	20	13	350	0	1150	70	18296	0	33795	968	0.304	0.345	459
SB16-113_spot8	1354	1550	1588	1625	49	70	27	20	160	0	510	43	10724	0	19534	915	0.314	0.344	463
SB16-113_spot5	1353	1550	1588	1629	49	70	19	15	400	0	1800	57	23827	0	50251	909	0.222	0.318	465
SB16-113_spot2	1357	1550	1588	1624	47	70	27	15	285	0	1020	57	18323	0	40465	909	0.279	0.307	493
SB16-113_spot16	1356	1550	1591	1624	47	70	31	20	125	0	320	65	7738	0	15079	1383	0.391	0.320	509
SB16-113_spot3	1358	1550	1590	1625	40	70	29	15	100	0	290	20	5877	0	13210	319	0.345	0.303	515
SB16-113_spot1	1357	1550	1590	1625	40	70	25	14	180	0	810	55	9483	0	29240	819	0.222	0.240	548
SB16-113_spot13	1357	1550	1589	1627	45	70	20	14	115	0	840	25	7341	0	26389	372	0.137	0.215	550
SB16-113_spot14	1356	1550	1588	1629	70	70	19	20	25	0	350	5	2216	0	10108	106	0.071	0.178	570
																mean:	0.318	0.327	481
																1σ (internal):	0.117	0.068	45
																1 SE (internal):	0.030	0.018	12
																		propagated 2 SE (internal and external):	35
																		n:	15
SB16-89_spot17	1354	1550	1584	1621	51	70	18	18	35	0	245	25	2351	0	6480	479	0.143	0.253	512
SB16-89_spot14	1356	1550	1584	1624	48	70	15	14	38	0	380	20	2588	0	8954	298	0.100	0.219	535
SB16-89_spot16	1341	1550	1584	1620	55	70	17	18	21	0	260	6	1814	0	6943	115	0.081	0.204	545
SB16-89_spot18	1351	1550	1584	1621	43	70	18	18	41	0	350	0	2322	0	9310	0	0.117	0.200	560
SB16-89_spot8	1354	1550	1584	1622	38	70	20	14	75	0	980	0	4332	0	30788	0	0.077	0.123	630
SB16-89_spot3	1362	1550	1585	1626	90	70	15	15	12	0	535	0	1423	0	12606	0	0.022	0.101	637
SB16-89_spot12	1346	1550	1584	1622	59	70	18	14	59	0	1480	0	4762	0	40495	0	0.040	0.105	638
SB16-89_spot10	1355	1550	1584	1622	60	70	18	14	45	0	1100	0	3556	0	30600	0	0.041	0.104	639
SB16-89_spot9	1345	1550	1583	1622	65	70	17	14	32	0	1000	0	2845	0	26704	0	0.032	0.096	645
SB16-89_spot11	1351	1550	1584	1622	50	70	18	14	41	0	1080	0	2596	0	29550	0	0.038	0.081	663
SB16-89_spot4	1365	1550	1584	1626	80	70	17	15	14	0	1060	0	1759	0	27473	0	0.013	0.060	677
SB16-89_spot7	1360	1550	1586	1622	40	70	17	14	32	0	1300	0	2011	0	33593	0	0.025	0.057	685
SB16-89_spot6	1370	1550	1584	1622	60	70	17	14	7	0	570	0	660	0	15221	0	0.012	0.042	697
SB16-89_spot2	1354	1550	1585	1626	60	70	16	15	10	0	1000	0	790	0	23561	0	0.010	0.033	706
																mean:	0.054	0.120	626
																1σ (internal):	0.041	0.068	61
																1 SE (internal):	0.011	0.018	16
																		propagated 2 SE (internal and external):	42
																		n:	14
SB16-91_spot16	1352	1550	1583	1623	42	70	16	12	160	0	510	40	9192	0	12818	510	0.314	0.408	395
SB16-91_spot11	1351	1550	1582	1623	45	70	23	17	263	0	690	100	17390	0	24929	1808	0.381	0.394	427

SB16-91_spot13	1353	1550	1582	1620	40	70	19	18	310	0	790	105	15703	0	22816	2010	0.392	0.387	438
SB16-91_spot10	1353	1550	1581	1620	43	70	27	15	184	0	450	20	10421	0	17236	319	0.409	0.373	457
SB16-91_spot4	1352	1550	1582	1621	45	70	23	15	315	0	1150	40	20828	0	40206	638	0.274	0.338	459
SB16-91_spot18	1355	1550	1582	1624	46	70	18	14	148	0	990	55	8622	0	27088	819	0.162	0.281	487
SB16-91_spot9	1353	1550	1581	1621	44	70	25	18	122	0	600	0	8432	0	22040	0	0.203	0.277	504
SB16-91_spot12	1351	1550	1583	1621	42	70	20	21	135	0	860	55	8187	0	27018	1228	0.157	0.225	546
SB16-91_spot6	1355	1550	1583	1621	65	70	18	18	18	0	330	10	1482	0	9071	191	0.055	0.138	607
SB16-91_spot8	1358	1550	1582	1621	52	70	15	18	55	0	1210	0	4202	0	27129	0	0.046	0.134	609
SB16-91_spot7	1356	1550	1581	1621	61	70	17	18	22	0	950	0	2108	0	24549	0	0.023	0.079	660
SB16-91_spot3	1350	1550	1583	1626	45	70	19	18	48	0	1720	0	2955	0	46754	0	0.028	0.059	683
SB16-91_spot2	1360	1550	1583	1626	70	70	15	18	13	0	1150	0	1199	0	24501	0	0.011	0.047	691
SB16-91_spot17	1343	1550	1582	1623	45	70	16	12	22	0	1230	0	1455	0	29915	0	0.018	0.046	694
SB16-91_spot14	1355	1550	1583	1616	60	70	15	23	10	0	830	20	821	0	18925	489	0.012	0.041	698
SB16-91_spot15	1357	1550	1582	1616	40	70	16	23	15	0	1210	0	942	0	30411	0	0.012	0.030	709
																mean:	0.156	0.204	566
																1σ (internal):	0.148	0.142	110
																1 SE (internal):	0.037	0.035	28
																		propagated 2 SE (internal and external):	61
																		n:	16
SB16-108_spot9	1352	1550	1589	1631	45	70	18	13	400	0	635	110	22339	0	17954	1521	0.630	0.534	338
SB16-108_spot15	1351	1550	1587	1625	46	70	21	15	282	0	385	35	15112	0	12290	558	0.732	0.540	353
SB16-108_spot8	1356	1550	1587	1629	42	70	19	12	700	0	1520	113	34249	0	40237	1442	0.461	0.451	387
SB16-108_spot5	1351	1550	1587	1626	38	70	19	14	290	0	690	30	15074	0	18930	447	0.420	0.438	391
SB16-108_spot2	1351	1550	1587	1624	41	70	18	13	400	0	980	48	19937	0	25199	664	0.408	0.435	391
SB16-108_spot13	1354	1550	1588	1630	45	70	17	10	350	0	1350	50	20345	0	32557	532	0.259	0.381	408
SB16-108_spot6	1346	1550	1588	1621	44	70	20	18	108	0	400	58	6982	0	11552	1110	0.270	0.355	439
SB16-108_spot17	1353	1550	1588	1626	41	70	20	13	140	0	445	25	7560	0	13077	346	0.315	0.360	446
SB16-108_spot3	1348	1550	1588	1622	45	70	21	18	240	0	780	60	13677	0	24068	1149	0.308	0.352	453
SB16-108_spot18	1354	1550	1588	1632	43	70	20	18	103	0	390	11	5834	0	11856	211	0.264	0.326	469
SB16-108_spot4	1349	1550	1587	1623	41	70	24	16	170	0	665	75	10241	0	22641	1276	0.256	0.300	494
SB16-108_spot1	1353	1550	1588	1625	42	70	20	15	315	0	1345	40	16754	0	41572	638	0.234	0.284	505
SB16-108_spot16	1354	1550	1588	1628	46	70	21	15	140	0	680	10	7829	0	21707	160	0.206	0.264	518
SB16-108_spot14	1337	1550	1588	1624	16	70	19	15	450	0	590	10	9666	0	17040	160	0.763	0.360	551
SB16-108_spot7	1362	1550	1589	1630	42	70	24	14	200	0	1950	90	11490	0	66390	1340	0.103	0.145	615
																mean:	0.375	0.368	450
																1σ (internal):	0.189	0.099	74
																1 SE (internal):	0.049	0.026	19
																		propagated 2 SE (internal and external):	46
																		n:	15
SB16-105_spot6	1350	1550	1589	1619	55	70	33	21	87	0	135	25	6788	0	6998	558	0.644	0.473	406
SB16-105_spot9	1356	1550	1589	1620	51	70	27	23	115	0	245	45	8023	0	9720	1101	0.469	0.426	416
SB16-105_spot7	1359	1550	1589	1621	51	70	31	19	49	0	89	20	3418	0	4194	404	0.551	0.426	435
SB16-105_spot2	1357	1550	1588	1624	53	70	33	16	93	0	200	23	7242	0	10367	391	0.465	0.402	440
SB16-105_spot1	1358	1550	1588	1621	52	70	33	15	95	0	205	35	7258	0	10626	558	0.463	0.394	448
SB16-105_spot5	1358	1550	1590	1625	51	70	29	21	135	0	265	40	8370	0	11682	893	0.509	0.400	453
SB16-105_spot4	1357	1550	1590	1623	53	70	35	19	52	0	100	20	3770	0	5498	404	0.520	0.390	466
SB16-105_spot3	1359	1550	1590	1626	51	70	35	16	87	0	185	35	6519	0	10171	596	0.470	0.377	468
SB16-105_spot8	1356	1550	1589	1624	49	70	34	23	68	0	135	23	4727	0	7210	563	0.504	0.378	475
																mean:	0.511	0.407	445
																1σ (internal):	0.055	0.029	22
																1 SE (internal):	0.018	0.010	7
																		propagated 2 SE (internal and external):	37
																		n:	9
SB16-97_spot4	1356	1550	1588	1628	62	70	18	35	50	0	1500	35	4869	0	42412	1303	0.167	0.280	490
SB16-97_spot18	1356	1550	1588	1624	46	70	18	18	90	0	730	95	5663	0	19307	1819	0.123	0.211	550
SB16-97_spot13	1350	1550	1588	1621	42	70	17	18	200	0	1800	135	11490	0	44962	2584	0.111	0.195	564
SB16-97_spot3	1358	1550	1589	1625	75	70	18	15	24	0	600	10	2827	0	16965	160	0.040	0.142	598
SB16-97_spot17	1353	1550	1587	1623	44	70	18	18	145	0	1840	80	8403	0	47824	1531	0.079	0.145	607
SB16-97_spot11	1356	1550	1588	1626	40	70	17	18	150	0	1870	35	7903	0	48323	670	0.080	0.139	614
SB16-97_spot12	1357	1550	1588	1625	37	70	16	19	70	0	1130	36	3806	0	28400	727	0.062	0.116	633
SB16-97_spot2	1356	1550	1588	1628	62	70	18	35	50	0	1500	35	4869	0	42412	1303	0.033	0.100	641
SB16-97_spot1	1352	1550	1588	1626	55	70	14	15	70	0	2520	55	5657	0	51838	877	0.028	0.097	643
SB16-97_spot14	1358	1550	1589	1623	36	70	18	18	75	0	980	80	3419	0	25919	1531	0.077	0.111	643
SB16-97_spot6	1364	1550	1589	1624	38	70	18	14	31	0	395	28	1432	0	11168	417	0.078	0.110	644
SB16-97_spot5	1361	1550	1589	1620	38	70	17	16	35	0	630	32	1819	0	16280	544	0.056	0.098	651
SB16-97_spot15	1360	1550	1589	1626	36	70	17	15	45	0	880	18	2380	0	22740	287	0.051	0.094	654
SB16-97_spot10	1359	1550	1588	1621	50	70	16	15	25	0	780	21	1773	0	18654	335	0.032	0.085	656
SB16-97_spot16	1357	1550	1589	1625	38	70	17	16	93	0	1800	30	4296	0	46514	510	0.052	0.084	664
SB16-97_spot7	1358	1550	1589	1619	45	70	16	15	12	0	580	25	602	0	14106	399	0.021	0.040	701
																mean:	0.068	0.128	622
																1σ (internal):	0.038	0.057	50
																1 SE (internal):	0.009	0.014	12
																		propagated 2 SE (internal and external):	35
																		n:	16
SB16-99_spot14	1338	1550	1586	1624	85	70	20	20	48	0	300	18	5995	0	9120	383	0.160	0.387	374

48

SB16-99_spot4	1346	1550	1585	1620	48	70	20	20	45	0	250	15	3393	0	7600	319	0.180	0.300	472
SB16-99_spot5	1348	1550	1585	1624	65	70	19	19	35	0	350	10	3574	0	9771	202	0.100	0.264	487
SB16-99_spot9	1356	1550	1585	1619	48	70	20	18	75	0	700	35	5472	0	20571	670	0.107	0.205	552
SB16-99_spot17	1355	1550	1585	1620	45	70	19	10	80	0	810	15	4924	0	23394	160	0.099	0.173	584
SB16-99_spot15	1353	1550	1584	1622	41	70	19	18	170	0	1600	50	9888	0	46210	957	0.106	0.173	586
SB16-99_spot7	1356	1550	1585	1621	43	70	19	15	95	0	1170	25	5795	0	32663	399	0.081	0.149	604
SB16-99_spot18	1354	1550	1585	1620	43	70	20	19	100	0	1340	35	6100	0	38394	707	0.075	0.135	617
SB16-99_spot13	1357	1550	1586	1618	52	70	20	20	30	0	570	40	2371	0	16172	851	0.053	0.122	624
SB16-99_spot8	1356	1550	1585	1620	48	70	20	17	65	0	1200	35	4584	0	35264	633	0.054	0.113	634
SB16-99_spot1	1335	1550	1585	1621	110	70	16	14	30	0	1790	20	4514	0	42082	298	0.017	0.096	640
SB16-99_spot6	1359	1550	1585	1624	40	70	19	19	50	0	1170	0	3142	0	32663	0	0.043	0.088	657
SB16-99_spot2	1362	1550	1585	1616	41	70	17	22	32	0	860	62	1795	0	21852	1451	0.037	0.072	673
																mean:	0.085	0.175	577
																1σ (internal):	0.045	0.089	83
																1 SE (internal):	0.013	0.025	23
																propagated 2 SE (internal and external):			54
																n:			13
SB16-101_spot3	1348	1550	1588	1621	43	70	28	18	175	0	340	55	11820	0	13505	1053	0.515	0.448	403
SB16-101_spot9	1353	1550	1587	1627	44	70	26	15	235	0	480	48	14144	0	18337	766	0.490	0.425	422
SB16-101_spot12	1354	1550	1588	1626	43	70	25	20	360	0	990	65	23531	0	35110	1383	0.364	0.392	425
SB16-101_spot10	1355	1550	1589	1628	41	70	25	20	680	0	1350	110	35307	0	47878	2340	0.504	0.413	438
SB16-101_spot13	1356	1550	1589	1625	44	70	24	21	430	0	1300	80	27800	0	45843	1787	0.331	0.369	441
SB16-101_spot8	1356	1550	1589	1629	42	70	28	16	255	0	530	37	14650	0	22558	630	0.481	0.387	460
SB16-101_spot2	1358	1550	1589	1628	40	70	26	16	330	0	845	65	18726	0	32281	1106	0.391	0.359	467
SB16-101_spot7	1357	1550	1588	1626	39	70	25	16	320	0	890	60	16438	0	31564	1021	0.360	0.335	485
SB16-101_spot4	1355	1550	1588	1629	44	70	26	18	165	0	630	25	10667	0	23237	479	0.262	0.310	485
SB16-101_spot14	1355	1550	1589	1624	48	70	24	19	150	0	760	100	11310	0	25875	2021	0.197	0.288	490
SB16-101_spot6	1357	1550	1588	1626	42	70	22	18	145	0	680	25	8639	0	21482	479	0.213	0.282	501
SB16-101_spot11	1356	1550	1589	1627	46	70	30	15	267	0	940	70	16800	0	40004	1117	0.284	0.290	513
SB16-101_spot1	1357	1550	1588	1628	39	70	26	14	450	0	1710	80	24896	0	65326	1191	0.263	0.272	526
SB16-101_spot16	1358	1550	1588	1627	41	70	21	21	290	0	1500	80	16264	0	46284	1787	0.193	0.253	526
SB16-101_spot18	1358	1550	1587	1627	38	70	20	20	280	0	1710	55	15634	0	51986	1170	0.164	0.227	546
SB16-101_spot17	1358	1550	1588	1628	40	70	18	23	180	0	1950	50	10214	0	53354	1223	0.092	0.158	598
																mean:	0.319	0.326	483
																1σ (internal):	0.128	0.077	50
																1 SE (internal):	0.032	0.019	13
																propagated 2 SE (internal and external):			35
																n:			16
SB16-103_spot11	1352	1550	1589	1622	50	70	29	19	270	0	430	120	21206	0	19588	2425	0.628	0.491	383
SB16-103_spot13	1354	1550	1590	1625	52	70	31	24	550	0	710	205	36219	0	34573	5232	0.775	0.476	430
SB16-103_spot12	1353	1550	1589	1624	51	70	31	24	450	0	750	170	30228	0	35341	4339	0.600	0.432	440
SB16-103_spot10	1356	1550	1589	1624	48	70	28	20	550	0	1170	120	36112	0	51459	2552	0.470	0.401	442
SB16-103_spot2	1357	1550	1589	1625	44	70	17	20	150	0	850	45	10032	0	21965	957	0.176	0.304	467
SB16-103_spot15	1360	1550	1588	1622	48	70	22	14	60	0	340	10	3501	0	11370	149	0.176	0.233	543
SB16-103_spot16	1357	1550	1587	1624	40	70	25	16	44	0	230	10	2407	0	8157	170	0.191	0.228	552
SB16-103_spot7	1356	1550	1588	1625	46	70	24	15	95	0	800	38	6864	0	27237	606	0.119	0.198	563
SB16-103_spot8	1353	1550	1589	1620	46	70	24	22	75	0	670	60	5069	0	22811	1404	0.112	0.173	588
SB16-103_spot1	1355	1550	1588	1626	46	70	19	18	75	0	1300	15	5419	0	37546	287	0.058	0.125	622
SB16-103_spot3	1358	1550	1588	1627	44	70	18	15	65	0	1180	20	4492	0	31747	319	0.055	0.123	623
																mean:	0.305	0.289	514
																1σ (internal):	0.249	0.132	80
																1 SE (internal):	0.075	0.040	24
																propagated 2 SE (internal and external):			57
																n:			11
LP-53_spot8	1325	1550	1586	1620	85	70	30	18	460	0	380	70	48524	0	16172	1340	1.211	0.735	223
LP-53_spot14	1326	1550	1587	1623	90	70	31	22	830	0	730	190	98390	0	34399	4445	1.137	0.717	233
LP-53_spot3	1327	1550	1589	1623	100	70	35	24	650	0	400	190	83965	0	21991	4849	1.625	0.758	237
LP-53_spot1	1325	1550	1587	1622	77	70	28	25	1030	0	1150	290	96415	0	42412	7710	0.896	0.658	258
LP-53_spot15	1330	1550	1587	1622	75	70	31	20	1250	0	1240	280	137750	0	60381	5955	1.008	0.675	259
LP-53_spot2	1327	1550	1587	1624	80	70	29	23	870	0	1050	260	88142	0	43196	6360	0.829	0.640	265
LP-53_spot16	1330	1550	1586	1619	74	70	30	22	530	0	480	170	55637	0	22619	3977	1.104	0.677	271
LP-53_spot12	1341	1550	1585	1621	53	70	31	21	630	0	900	170	50924	0	39579	3797	0.700	0.563	322
LP-53_spot11	1353	1550	1588	1626	46	70	34	20	108	0	110	15	7804	0	5116	319	0.982	0.589	346
LP-53_spot13	1343	1550	1585	1623	48	70	30	20	1070	0	1365	240	80676	0	60169	5105	0.784	0.553	349
LP-53_spot9	1341	1550	1586	1620	49	70	29	21	700	0	900	190	48658	0	35701	4243	0.778	0.549	352
LP-53_spot6	1351	1550	1588	1623	40	70	28	26	875	0	525	155	47875	0	21972	4286	1.667	0.646	359
LP-53_spot4	1351	1550	1588	1622	38	70	28	24	870	0	520	145	45222	0	21393	3701	1.673	0.643	362
LP-53_spot10	1351	1550	1586	1625	38	70	28	17	115	0	170	20	6421	0	6511	362	0.676	0.483	402
LP-53_spot17	1353	1550	1586	1622	36	70	26	21	670	0	1060	150	32993	0	40495	3350	0.632	0.429	450
LP-53_spot18	1354	1550	1586	1623	40	70	30	22	950	0	1550	160	50051	0	70683	3743	0.613	0.402	475
																mean:	1.020	0.607	323
																1σ (internal):	0.351	0.102	75
																1 SE (internal):	0.088	0.025	19
																propagated 2 SE (internal and external):			45
																n:			16

49

LP-52_spot1	1332	1550	1586	1622	63	70	26	20	1270	0	1770	270	117561	0	69953	5743	0.718	0.608	277
LP-52_spot3	1346	1550	1586	1621	54	70	30	23	745	0	670	155	61152	0	30553	4696	1.112	0.634	318
LP-52_spot2	1344	1550	1585	1621	52	70	30	24	610	0	500	130	48216	0	22801	4109	1.220	0.642	324
LP-52_spot17	1353	1460	1586	1619	49	55	31	25	1680	0	1590	390	125132	0	77425	12347	1.057	0.618	327
LP-52_spot13	1339	1460	1586	1622	55	55	26	21	1270	0	2380	250	106176	0	94062	6116	0.534	0.515	336
LP-52_spot6	1353	1550	1586	1619	46	70	33	26	1550	0	1020	320	111998	0	52873	10959	1.520	0.637	359
LP-52_spot11	1351	1470	1588	1620	45	75	35	21	1080	0	690	250	71410	0	35484	5583	1.565	0.635	364
LP-52_spot18	1353	1460	1587	1620	48	55	34	28	2100	0	1570	410	153222	0	83849	13373	1.338	0.612	369
LP-52_spot12	1351	1460	1587	1620	51	55	37	22	2300	70	1850	450	178303	4094	107521	11533	1.243	0.600	371
LP-52_spot7	1352	1470	1586	1619	51	75	38	27	1740	55	1200	390	139392	4387	71628	13869	1.450	0.620	372
LP-52_spot8	1352	1470	1587	1620	48	75	38	27	1600	0	1270	320	120637	0	70910	9188	1.260	0.601	372
LP-52_spot15	1352	1460	1587	1620	42	55	34	25	1960	0	1200	390	123044	0	62019	11358	1.633	0.626	378
LP-52_spot14	1353	1460	1587	1622	40	55	32	22	990	0	770	200	59190	0	36204	5126	1.286	0.589	388
LP-52_spot16	1350	1460	1586	1618	49	55	44	23	3670	0	2300	590	273353	0	158965	15808	1.596	0.610	393
LP-52_spot5	1353	1550	1586	1620	43	70	31	25	660	0	630	165	44579	0	30678	5433	1.048	0.552	396
LP-52_spot4	1349	1550	1586	1620	44	70	36	25	1340	0	950	270	89623	0	53721	8891	1.411	0.589	401
																mean:	1.249	0.606	359
																1σ (internal):	0.297	0.032	33
																1 SE (internal):	0.074	0.008	8
																		propagated 2 SE (internal and external):	30
																		n:	16
LP-50_spot6	1350	1530	1599	1620	68	70	50	17	2220	80	1420	310	237127	5955	100721	5604	1.563	0.690	306
LP-50_spot8	1348	1500	1585	1623	44	80	22	18	540	10	730	120	37322	851	25227	2297	0.740	0.576	316
LP-50_spot5	1347	1525	1601	1622	68	75	52	17	4800	150	3030	500	512708	11964	231508	9040	1.584	0.681	317
LP-50_spot1	1350	1520	1598	1625	64	80	55	25	3550	120	2100	400	356885	10209	157989	10635	1.690	0.679	325
LP-50_spot7	1351	1530	1597	1621	61	70	55	18	2250	43	1320	340	215592	3201	102990	6508	1.705	0.677	328
LP-50_spot2	1350	1520	1599	1621	61	80	55	20	4100	120	2470	430	386512	10209	185825	9146	1.660	0.665	338
LP-50_spot4	1352	1470	1596	1621	56	70	58	17	2780	70	1400	240	244542	5211	119310	4339	1.986	0.664	348
LP-50_spot14	1350	1480	1597	1621	54	75	55	21	2000	10	1000	250	169646	798	86394	5583	2.000	0.663	349
LP-50_spot10	1349	1530	1598	1620	64	80	55	21	3870	20	2230	520	389055	1702	192658	11613	1.735	0.656	351
LP-50_spot11	1351	1540	1597	1622	57	70	53	22	3120	20	1600	450	279350	1489	133204	10528	1.950	0.660	352
LP-50_spot13	1352	1480	1591	1620	55	75	49	24	2420	40	1240	550	209073	3190	95442	14038	1.952	0.656	356
LP-50_spot12	1352	1530	1596	1621	55	70	49	21	1990	25	1050	350	166371	1861	80817	7817	1.895	0.652	360
LP-50_spot15	1350	1480	1596	1620	53	75	53	20	4540	20	2300	580	377965	1595	191480	12336	1.974	0.650	363
LP-50_spot3	1352	1480	1598	1620	56	80	57	20	1200	40	660	180	102148	3403	55276	3829	1.818	0.633	379
LP-50_spot9	1351	1500	1595	1621	56	80	55	21	2260	10	1350	400	192379	851	116632	8933	1.674	0.605	403
																mean:	1.728	0.654	346
																1σ (internal):	0.302	0.029	25
																1 SE (internal):	0.078	0.007	6
																		propagated 2 SE (internal and external):	29
																		n:	15
LP-42_spot14	1344	1525	1603	1619	90	100	50	20	3450	250	2950	380	487732	26587	201760	8082	1.169	0.699	256
LP-42_spot13	1344	1530	1603	1620	90	110	53	20	5500	430	5000	480	777544	50302	349041	10209	1.100	0.690	256
LP-42_spot8	1342	1525	1604	1622	87	105	53	19	5450	380	4500	600	744793	42433	320186	12124	1.211	0.699	262
LP-42_spot5	1345	1530	1604	1622	87	100	50	20	4200	320	3660	450	573969	34031	250320	9571	1.148	0.688	265
LP-42_spot18	1344	1525	1604	1619	81	105	53	21	3950	270	3220	120	502576	30149	216124	2680	1.227	0.697	266
LP-42_spot11	1346	1530	1603	1620	78	110	51	20	4430	210	3080	500	542773	24566	206895	10635	1.438	0.714	270
LP-42_spot10	1344	1520	1604	1621	88	110	55	19	6900	610	6100	450	953788	71359	450409	9093	1.131	0.679	273
LP-42_spot2	1348	1530	1605	1620	80	100	50	20	3480	230	2790	130	437310	24460	190817	2765	1.247	0.693	273
LP-42_spot7	1350	1530	1604	1623	82	105	50	20	4700	420	3900	580	605385	46899	266734	12336	1.205	0.684	277
LP-42_spot1	1338	1480	1600	1619	83	75	50	19	2070	0	1460	190	269879	0	109113	3839	1.418	0.705	278
LP-42_spot3	1344	1520	1600	1621	75	100	53	20	3980	170	2420	550	468883	18079	181950	11698	1.645	0.720	279
LP-42_spot9	1343	1525	1603	1622	84	115	53	19	4450	380	3650	530	587164	46474	264614	10709	1.219	0.681	282
LP-42_spot15	1345	1530	1604	1619	79	110	53	20	2600	160	2050	150	322642	18717	148619	3190	1.268	0.685	284
LP-42_spot6	1344	1520	1601	1623	82	110	50	20	5260	420	4050	1050	677516	49132	287266	22333	1.299	0.686	286
LP-42_spot16	1345	1530	1600	1620	79	110	55	20	850	40	670	80	105479	4679	50406	1702	1.269	0.669	301
																mean:	1.266	0.693	274
																1σ (internal):	0.136	0.013	12
																1 SE (internal):	0.035	0.003	3
																		propagated 2 SE (internal and external):	26
																		n:	15
LP-37_spot4	1348	1520	1595	1621	110	110	62	22	3120	350	2600	200	539097	56569	216411	4679	1.200	0.709	250
LP-37_spot1	1350	1540	1604	1621	75	105	53	22	5270	360	3450	320	620857	49788	222285	7487	1.528	0.730	260
LP-37_spot7	1348	1520	1596	1619	105	110	62	20	1550	250	1180	200	255647	40407	100073	4254	1.314	0.710	262
LP-37_spot11	1348	1510	1594	1618	103	120	65	21	2800	450	2100	200	453018	84823	186714	4467	1.333	0.703	272
LP-37_spot6	1348	1525	1601	1620	81	110	53	22	3620	270	2400	450	460589	43639	170766	10528	1.508	0.718	272
LP-37_spot3	1349	1515	1597	1623	92	110	61	26	4760	500	3590	350	687883	80813	293994	9678	1.326	0.701	273
LP-37_spot15	1350	1505	1597	1620	93	110	60	21	6700	750	4750	700	978763	121220	389842	15633	1.411	0.707	275
LP-37_spot13	1350	1515	1601	1621	87	110	57	21	5000	420	3560	450	683296	67883	277568	10050	1.404	0.704	278
LP-37_spot5	1350	1525	1603	1620	76	110	55	22	4670	270	3060	350	557507	43639	225943	8189	1.526	0.712	280
LP-37_spot2	1350	1510	1597	1623	83	120	60	26	10270	1300	7700	1050	1338962	245044	561639	29033	1.334	0.694	281
LP-37_spot14	1350	1535	1602	1620	72	100	53	21	6080	350	3800	550	687632	51427	275488	12283	1.600	0.714	282
LP-37_spot18	1348	1520	1603	1620	73	110	54	20	6350	350	4160	500	728143	56569	307278	10635	1.526	0.696	297
LP-37_spot12	1346	1505	1602	1621	75	110	56	21	3400	210	2330	250	400553	33942	178479	5583	1.459	0.685	303
LP-37_spot9	1346	1505	1601	1619	80	110	65	20	1670	110	1120	100	209858	17779	99581	2127	1.491	0.678	313

																mean:	1.426	0.704	278
																1σ (internal):	0.108	0.013	16
																1 SE (internal):	0.029	0.003	4
																		propagated 2 SE (internal and external):	28
																		n:	14
LP-36_spot8	1347	1530	1600	1620	92	110	54	20	4250	470	3450	350	614181	54982	235931	7444	1.232	0.716	246
LP-36_spot13	1349	1530	1602	1620	80	105	52	20	6300	830	4350	550	791681	92682	291050	11698	1.448	0.731	253
LP-36_spot3	1349	1515	1602	1620	90	110	55	22	4200	330	3160	250	593761	38604	228918	5849	1.329	0.717	256
LP-36_spot15	1349	1535	1603	1621	76	105	51	20	6300	490	4320	600	752097	54716	283485	12762	1.458	0.726	259
LP-36_spot12	1349	1530	1603	1620	74	105	53	21	3870	280	2500	420	449845	31266	170487	9380	1.548	0.725	267
LP-36_spot9	1350	1520	1600	1620	87	115	57	20	5550	680	4130	450	758459	83164	304095	9571	1.344	0.707	269
LP-36_spot1	1345	1515	1599	1621	87	110	55	20	1900	180	1300	250	259653	21057	97802	5317	1.462	0.716	270
LP-36_spot10	1348	1530	1604	1620	73	115	53	20	4720	300	3150	300	541234	36690	214814	6381	1.498	0.716	273
LP-36_spot11	1348	1535	1604	1620	76	105	53	22	4500	340	3050	350	537212	37966	207994	8189	1.475	0.713	274
LP-36_spot14	1349	1535	1603	1620	75	110	54	20	6550	500	4480	550	771654	58491	311277	11698	1.462	0.705	282
LP-36_spot5	1347	1525	1604	1619	75	105	55	20	6600	420	4650	250	777544	46899	336857	5317	1.419	0.698	286
LP-36_spot7	1349	1525	1604	1620	76	115	54	20	3800	230	2630	250	453646	32154	194264	5317	1.445	0.700	286
LP-36_spot2	1351	1505	1600	1621	77	110	57	20	5850	400	4350	700	707565	46793	326583	14889	1.345	0.684	293
LP-36_spot4	1348	1520	1604	1620	75	110	57	22	4700	300	3240	300	553706	35095	243248	7019	1.451	0.689	298
LP-36_spot6	1349	1520	1604	1620	74	105	57	20	4630	240	3070	420	538186	26800	239363	8933	1.508	0.684	308
																mean:	1.428	0.708	275
																1σ (internal):	0.079	0.014	17
																1 SE (internal):	0.021	0.004	4
																		propagated 2 SE (internal and external):	27
																		n:	15

Discussion DR2: Analytical methods and supporting data for quartz petrofabric analyses

The orientations of quartz *c*-axes were measured on polished, foliation-normal, lineation-parallel thin sections using a Crystal Imaging Systems G60 automated crystal fabric analyzer from Russell-Head systems, housed at the University of British Columbia, Okanagan. Detailed descriptions of previous generation instruments that operate using the same theoretical approach are included in Wilson et al. (2007) and Peternell et al. (2010). The fabric analyzer determines the trend and plunge of the *c*-axis for each pixel in a composite image of the entire thin section, producing an achsenverteilungsanalyse (AVA) diagram (e.g., Sander, 1950) from which the user can build a spatially-referenced fabric using a variety of plane- and cross-polarized images to verify mineralogy. The orientations measured using this analytical method produce equivalent results to those measured using Electron BackScatter Diffraction, x-ray goniometry and neutron diffraction (e.g., Wilson et al., 2007; Peternell et al., 2010; Hunter et al. 2017).

Pole figures were generated using the program Orient (Vollmer, 2017), and were contoured using a Fourier transform of the entire orientation data set relative to multiples of a random distribution. Quartz *c*-axis fabric skeletons (Lister and Williams, 1979) were visually best-fit using the methods discussed in Law (2014). The opening angles of the crossed-girdle *c*-axis fabrics yielded by samples 3, 7, 14, and 82 were estimated by counting the degrees along the perimeter circle between the intersections of the fabric skeleton with the perimeter circle. The deformation temperature ranges reported for these samples were estimated using the pressure-independent calibration of Faleiros et al. (2016; their equation 1). Shear-sense on the pole plots for samples 3, 10, 14, and 21A was determined by asymmetry in the orientation of single- or crossed-girdle patterns relative to foliation, after Lister and Williams (1979) and Passchier and Trouw (2005). The bisector of the type II crossed-girdle yielded by Sample 82 is oriented approximately normal to foliation, and therefore could not be used to determine shear sense.

Discussion DR3: Analytical methods and supporting data for estimation of mean kinematic vorticity (W_m) using the quartz shape-preferred orientation (SPO) method of Wallis (1992; 1995)

In the case of plane-strain, monoclinic flow, quartz neoblasts are stretched in the direction of the instantaneous stretching axis (ISA_1) during and after dynamic recrystallization (e.g., Johnson et al., 2009) (Fig. DR1A). With continued strain, the long axes of deformed neoblasts progressively rotate toward the flow apophysis (AP1). The ISA_1 can be estimated by measuring the mean angle between foliation and the long axes of elongated quartz neoblasts (denoted here as θ'_{ISA1}). The AP_1 can be estimated by measuring the acute angle between foliation and the line normal to the central axis of a single- or crossed-girdle in a quartz *c* axis plot (denoted here as β, after Law et al., 2013) (Fig. DR1A). The angle between the ISA1 and the AP1 (denoted here as ζ, after Law et al., 2013), is equal to the sum of θ'_{ISA1} and β, and mean kinematic vorticity (W_m) is equal to $\sin(2\zeta)$ (Wallis, 1992; 1995).

We measured β by constructing a visual best-fit fabric skeleton of the *c*-axis plots (e.g., Lister and Williams, 1979) (see discussion above). For the four samples that exhibited a type I crossed girdle or a single girdle (3, 10, 14, 21A), β was measured as the acute angle between foliation and the line normal to central axis of the girdle (Figs. 9, DR1B). For sample 82, which yielded a type II crossed girdle, β was measured as the acute angle between foliation and the line normal to the bisector of the legs of the crossed girdle. β is reported as positive if it was inclined down to the SE relative to foliation, which is consistent with a top-to-SE shear sense. Conversely, if β was inclined down to the NW relative to foliation, which is consistent with a top-to-NW shear sense, it was reported as negative. For the five samples in which β was able to be measured, it varied between 1° and -18° (Fig. 9, Table 3).

After the procedure described in Long et al. (2016), we define the angle between the ISA_1 and foliation as θ'_{ISA1}, which we estimated using the mean value of θ' (defined as the acute angle measured between the long axis of a quartz neoblast and foliation; e.g., Ramsay and Huber, 1983) measurements from >100 adjacent quartz neoblasts. Grain boundaries were traced in Adobe Illustrator, with the areas of quartz neoblasts filled in solid white and any mineral phases other than quartz filled in solid black (Fig. DR2). This binary black-and-white image was imported into the program Image J (Schneider et al., 2012), and individual quartz neoblasts were modeled as ellipses using the 'fit ellipse' measurement tool. This generated an image of the fit ellipses (Fig. DR2), and a table of long axis length, short axis length, and long axis orientation data for each ellipse. The long axis orientation data were then used to populate θ' frequency histograms (Figs. 9E, DR3) for each analysis. The sign convention used for θ' is: clockwise from foliation is positive, and counterclockwise from foliation is negative. The reported θ'_{ISA1} is the mean of all θ' measurements, with ±1 standard error.

Figure DR1: Diagrams illustrating angles pertinent for estimating W_m using the quartz SPO method (modified from Long et al., 2016). A) Diagram of the kinematics of plane-strain, monoclinic deformation (modified from Johnson et al., 2009). ISA_1 and ISA_2 are the instantaneous stretching axes, and AP_1 and AP_2 are the flow apophyses. Relationships between β, θ'_{ISA1}, ζ, and W_m, as defined above, are shown. B) Illustration of determination of the β angle from a *c*-axis fabric skeleton (modified from Law et al., 2013). C) Illustration of determination of θ'_{ISA1} from a frequency histogram of all θ' measurements. θ'_{ISA1} is calculated as the mean of all measurements, and is reported with ± 1 standard error.

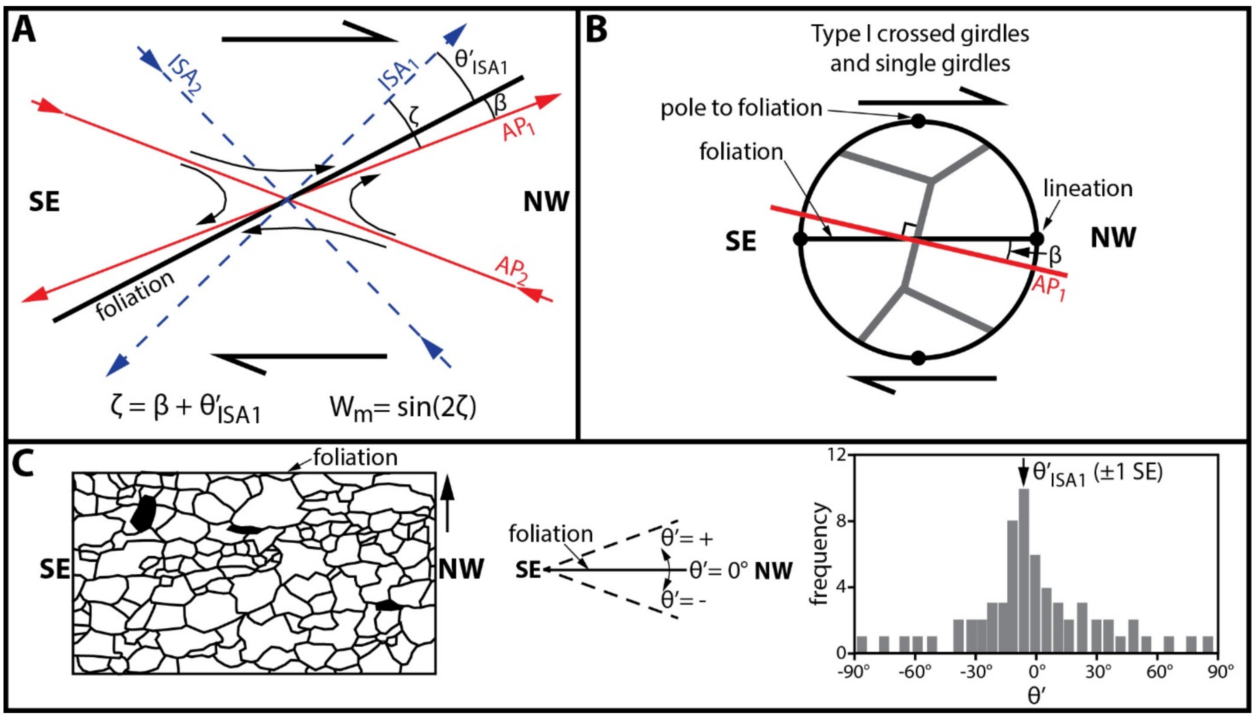

Figure DR2 (following page): Supporting figures for the estimation of θ'_{ISA1} from foliation-normal, lineation-parallel thin sections of samples 3, 10, 14, 21A, and 82. Three figures are shown for each sample: 1) A photomicrograph taken in cross-polarized light with a 540 nm λ plate inserted (oriented with foliation horizontal; view direction is toward the southwest); 2) a line trace of >100 adjacent, recrystallized quartz neoblasts (with white fill; phases other than quartz are shown with black fill); and 3) the ImageJ output figure after performing the 'fit ellipse' function.

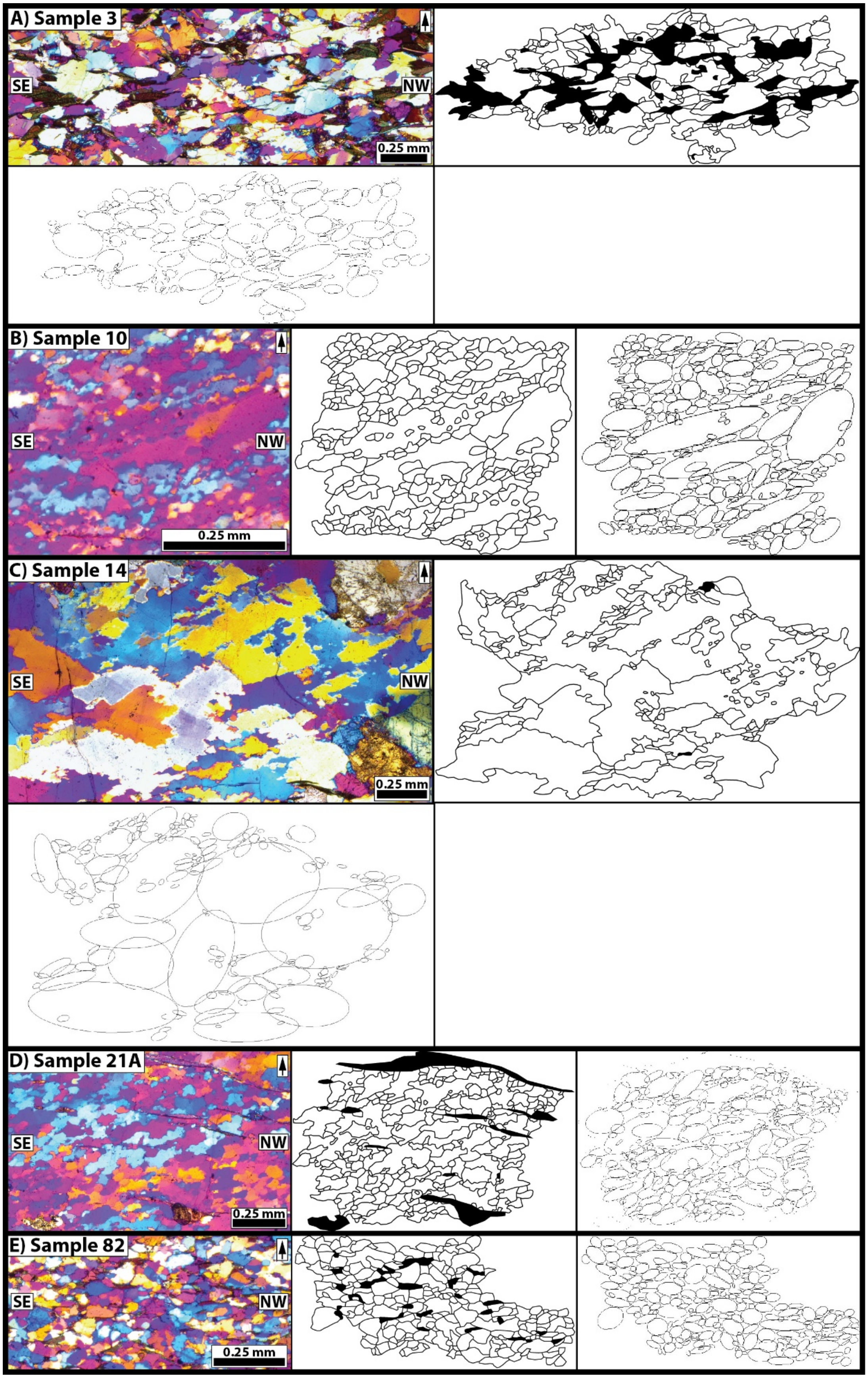
A) Sample 3
SE
NW
0.25 mm
B) Sample 10
SE
NW
0.25 mm
C) Sample 14
SE
NW
0.25 mm
D) Sample 21A
SE
NW
0.25 mm
E) Sample 82
SE
NW
0.25 mm

136

Figure DR3: Frequency histograms of θ' (the acute angle between foliation and the long axes of quartz neoblasts; e.g., Ramsay and Huber, 1983) in 1° increments for samples 3, 10, 14, 21A, and 82. θ'_{ISA1} is defined as the mean of all θ' measurements, ±1 standard error.

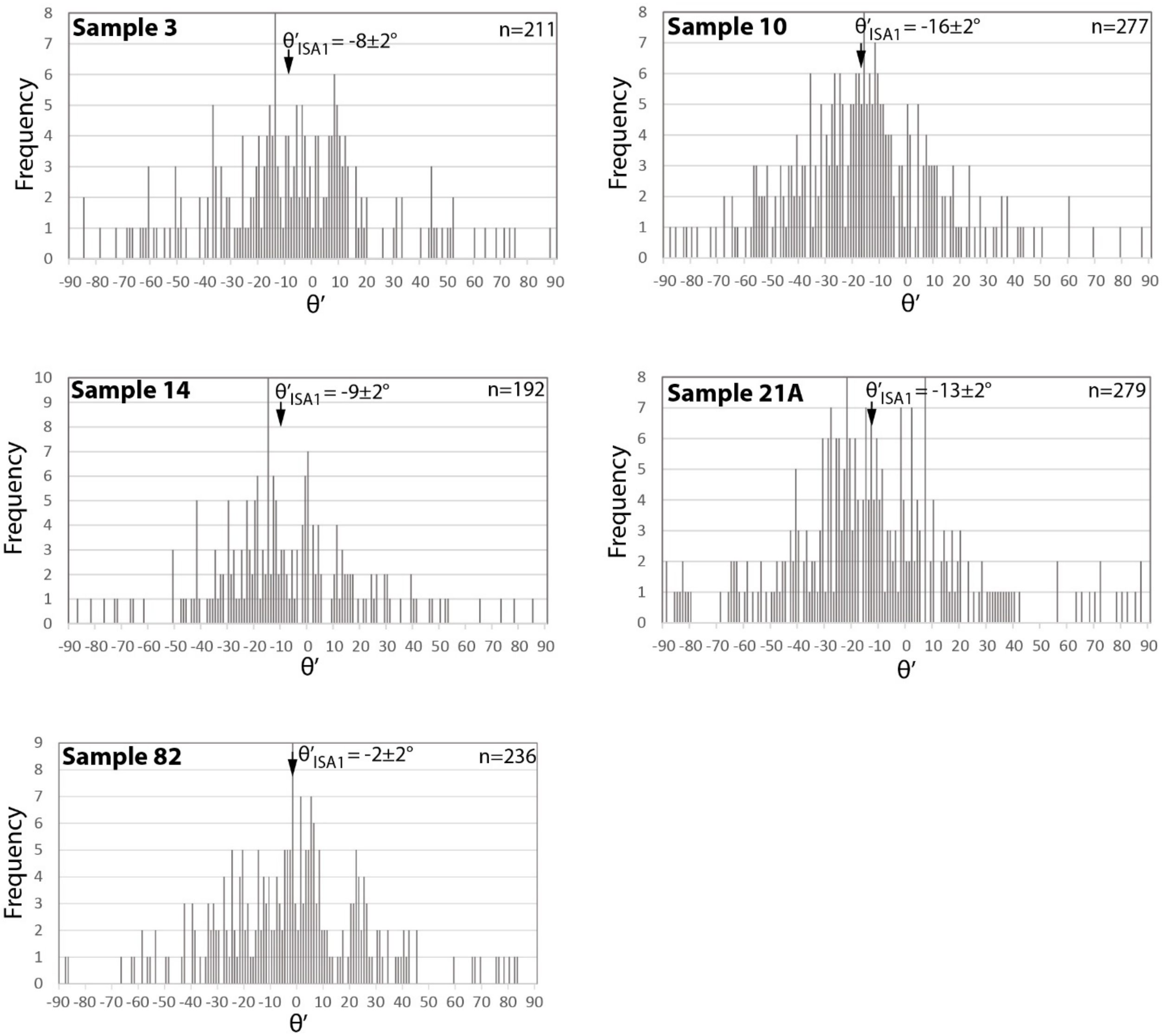

Discussion DR4: Analytical methods and supporting data for finite strain analyses

Two foliation-normal thin sections were analyzed from each finite strain sample (Tables 4, DR1), following methods outlined in Long et al. (2016; 2017). For the 22 samples that exhibited mineral stretching lineation, one thin section was cut parallel to lineation, which approximates the XZ strain plane (thin sections ending with ‘A’), and one was cut normal to lineation, which approximates the YZ strain plane (thin sections ending with ‘B’). For the three samples that exhibited crenulation cleavage but not stretching lineation, the ‘A’ thin section was cut normal to crenulation cleavage, and the ‘B’ thin section was cut parallel to crenulation cleavage.

For each thin section, the Rf-ϕ method (e.g., Ramsay, 1967; Dunnet, 1969; Ramsay and Huber, 1983) was used to quantify a 2D strain ellipse. The final elongation (Rf; the ratio of the long axis to the short axis), and ϕ (defined here as the angle of inclination of the long axis measured relative to foliation), were measured for ≥30 non-recrystallized quartz porphyroclasts on photomicrographs of each thin section. Photomicrographs were taken with the apparent dip of tectonic foliation oriented horizontal, NW or NE toward the right-hand side of the page, and structurally-upward toward the top of the page. Similar to the methods described above in Discussion DR3, grain boundaries were traced in Adobe Illustrator, with the areas of quartz porphyroclasts filled in solid white and all mineral phases other than quartz filled in solid black (Fig. DR4). This binary image was then imported into ImageJ (Schneider et al., 2012), and individual quartz porphyroclasts were modeled as ellipses using the ‘fit ellipse’ measurement tool. This generated an image of the fit ellipses (Fig. DR4), and a table of long axis length, short axis length, and long axis orientation (ϕ) for each grain, which were then used to populate the Rf-ϕ graphs (Fig. DR5). Representative photomicrographs, binary images, and fit ellipses are shown in Figure DR4, and Rf-ϕ plots showing data from individual grains measured on each thin section are shown in Figure DR5.

For all analyses, the mean of all ϕ values is reported as the overall ϕ value for the thin section. Analyses from 14 samples resembled ‘situation B’ of Figure 5.5 of Ramsay and Huber (1983); for these samples, the tectonic ellipticity (Rs) of each thin section was estimated using the harmonic mean of all Rf values (e.g., Lisle, 1977; 1979). Analyses from 11 samples resembled ‘situation A’ of Figure 5.5 of Ramsay and Huber (1983); for these samples, Rs was calculated using the equation $Rs = (Rf\ maximum/Rf\ minimum)^{1/2}$, with Rf maximum determined from a grain situated near the mean ϕ value and Rf minimum determined from a grain that was approximately 90° away from the mean ϕ value (Ramsay and Huber, 1983). Uncertainties reported for Rs and ϕ represent 1 standard error of all measurements (Rs values and uncertainties are rounded to the nearest single decimal place, and ϕ values and uncertainties are rounded to the nearest degree). Uncertainties in Rs range between ±0.1-0.3, and uncertainties in ϕ range between ±2-9°. ϕ was measured relative to the apparent dip of foliation, and is therefore equivalent to the parameter θ' defined by Ramsay and Huber (1983). The sign convention used for ϕ is: down to the NW or NE relative to foliation (clockwise from foliation in the photomicrographs) is positive, and down to the SE or SW relative to foliation (counterclockwise from foliation in the photomicrographs) is negative.

The Rs and ϕ values for the 2D strain ellipses from each 'A' and 'B' thin section were combined to generate the 3D strain ellipsoid for the sample (e.g., Long et al., 2016; 2017). For all analyses, the Z axis was assigned an Rs value of 1.0 in both ellipses, and the Rs values of both 2D ellipses were then directly compared to assign the X and Y strain directions (X>Y) and the relative magnitudes of the axes of the 3D strain ellipsoid. For all analyses, Rs in the 'A' thin section was either greater than or equivalent within error to Rs in the 'B' thin section, and in 39 of the 50 analyzed thin sections, the shortening direction is within 10° of normal to foliation. This justifies the use of macroscopic structural features, including foliation, lineation, and crenulation cleavage, to approximate the principal strain directions within the studied rocks. In addition, the quartz *c*-axis fabrics on Figure 9, by analogy with experiments and numerical modeling of fabric development, also demonstrate that stretching lineation in the analyzed samples is parallel to the maximum finite stretch (X) direction (e.g., Lister et al., 1978; Lister and Hobbs, 1980).

Figure DR4 (following page): Annotated photomicrographs showing representative examples of quartz grain measurements for Rf-ϕ analyses. All photomicrographs were taken in XPL, with foliation oriented horizontal (arrow points structurally-upward). Three figures are shown for each sample: 1) a photomicrograph; 2) a binary image of traced quartz porphyroclasts (with white fill; phases other than quartz are shown with black fill); and 3) the ImageJ output figure after performing the 'fit ellipse' function.

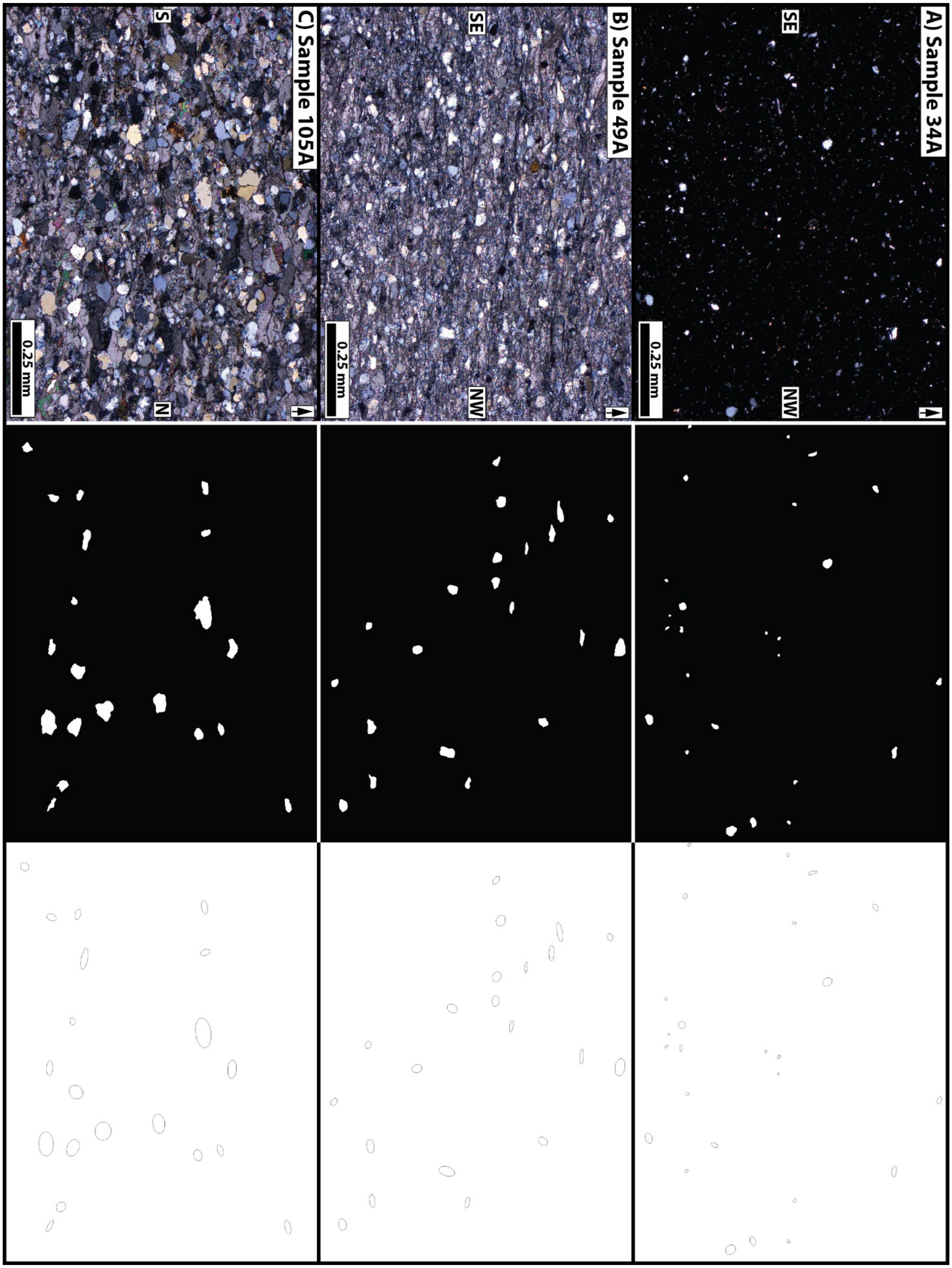
A) Sample 34A
SE
NW
0.25 mm
B) Sample 49A
SE
NW
0.25 mm
C) Sample 105A
S
N
0.25 mm

Figure DR5 (following 7 pages): Rf-ϕ graphs plotting the natural log of final ellipticity (Rf) versus the orientation of the long axis (ϕ) for individual quartz porphyroclasts. ϕ is measured relative to foliation; a positive ϕ value is down to the NW or NE relative to foliation (i.e., clockwise relative to foliation in the photomicrographs), and a negative ϕ value is down to the SE or SW relative to foliation (i.e., counterclockwise relative to foliation in the photomicrographs). Errors reported for Rs and ϕ represent 1 SE of all measurements. ‘Situation A’ and ‘Situation B’ refer to Figure 5.5 of Ramsay and Huber (1983). Refer to Table DR1 for a guide to abbreviated sample numbers used in the text.

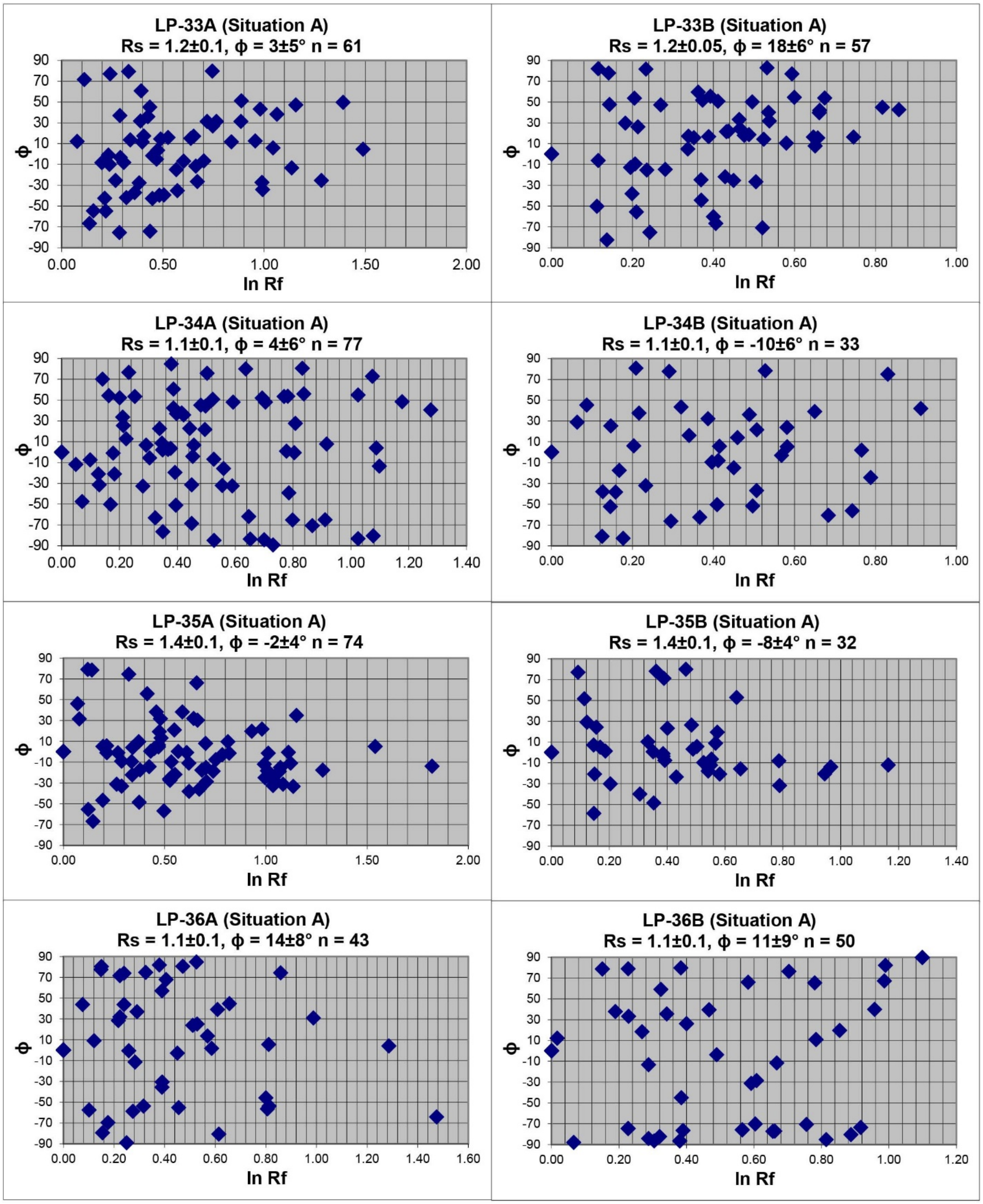
LP-33A (Situation A)
Rs = 1.2±0.1, ϕ = 3±5° n = 61
LP-33B (Situation A)
Rs = 1.2±0.05, ϕ = 18±6° n = 57
LP-34A (Situation A)
Rs = 1.1±0.1, ϕ = 4±6° n = 77
LP-34B (Situation A)
Rs = 1.1±0.1, ϕ = -10±6° n = 33
LP-35A (Situation A)
Rs = 1.4±0.1, ϕ = -2±4° n = 74
LP-35B (Situation A)
Rs = 1.4±0.1, ϕ = -8±4° n = 32
LP-36A (Situation A)
Rs = 1.1±0.1, ϕ = 14±8° n = 43
LP-36B (Situation A)
Rs = 1.1±0.1, ϕ = 11±9° n = 50
ϕ
ln Rf

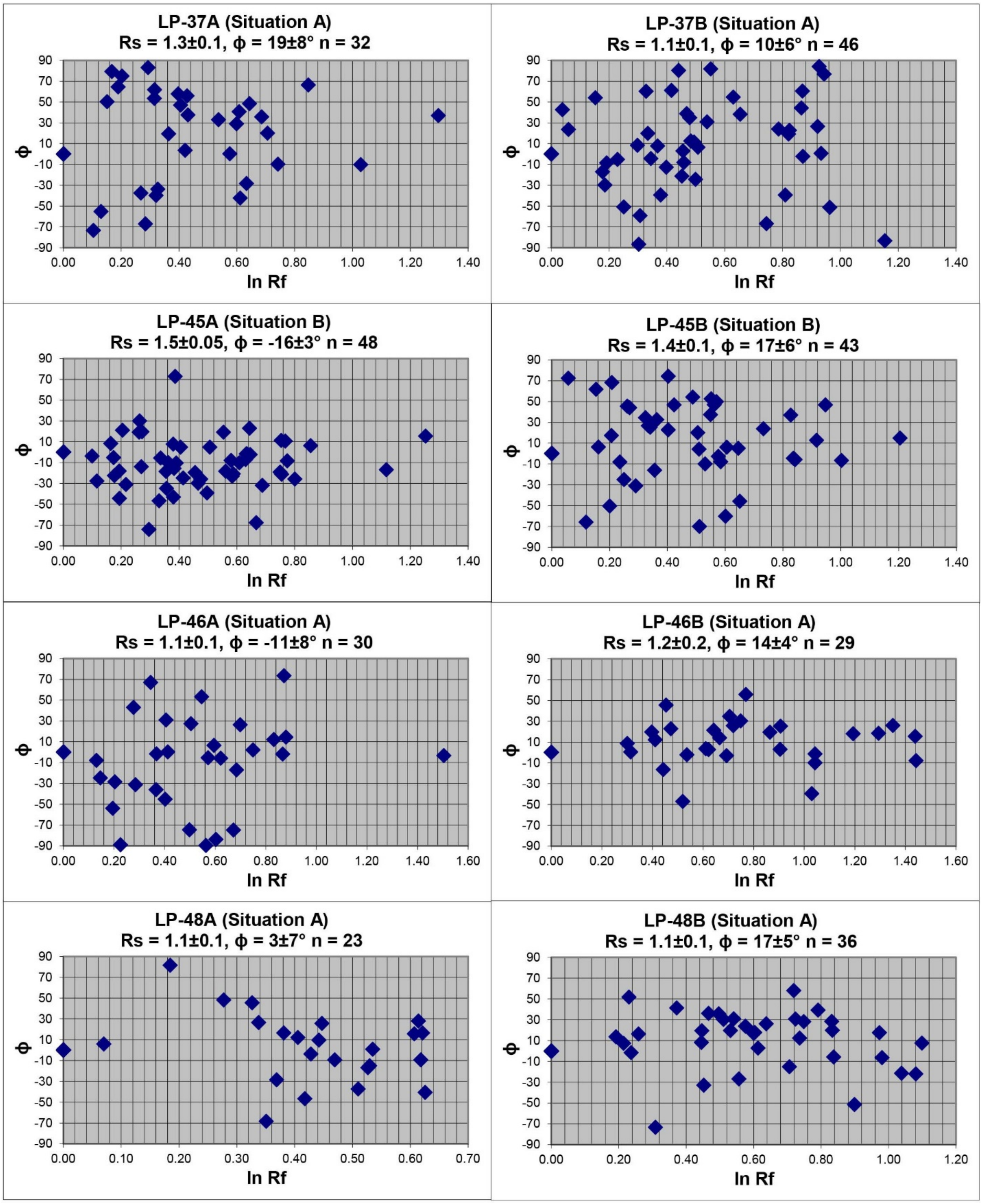
LP-37A (Situation A)
Rs = 1.3±0.1, ϕ = 19±8° n = 32
LP-37B (Situation A)
Rs = 1.1±0.1, ϕ = 10±6° n = 46
LP-45A (Situation B)
Rs = 1.5±0.05, ϕ = -16±3° n = 48
LP-45B (Situation B)
Rs = 1.4±0.1, ϕ = 17±6° n = 43
LP-46A (Situation A)
Rs = 1.1±0.1, ϕ = -11±8° n = 30
LP-46B (Situation A)
Rs = 1.2±0.2, ϕ = 14±4° n = 29
LP-48A (Situation A)
Rs = 1.1±0.1, ϕ = 3±7° n = 23
LP-48B (Situation A)
Rs = 1.1±0.1, ϕ = 17±5° n = 36
ϕ
ln Rf

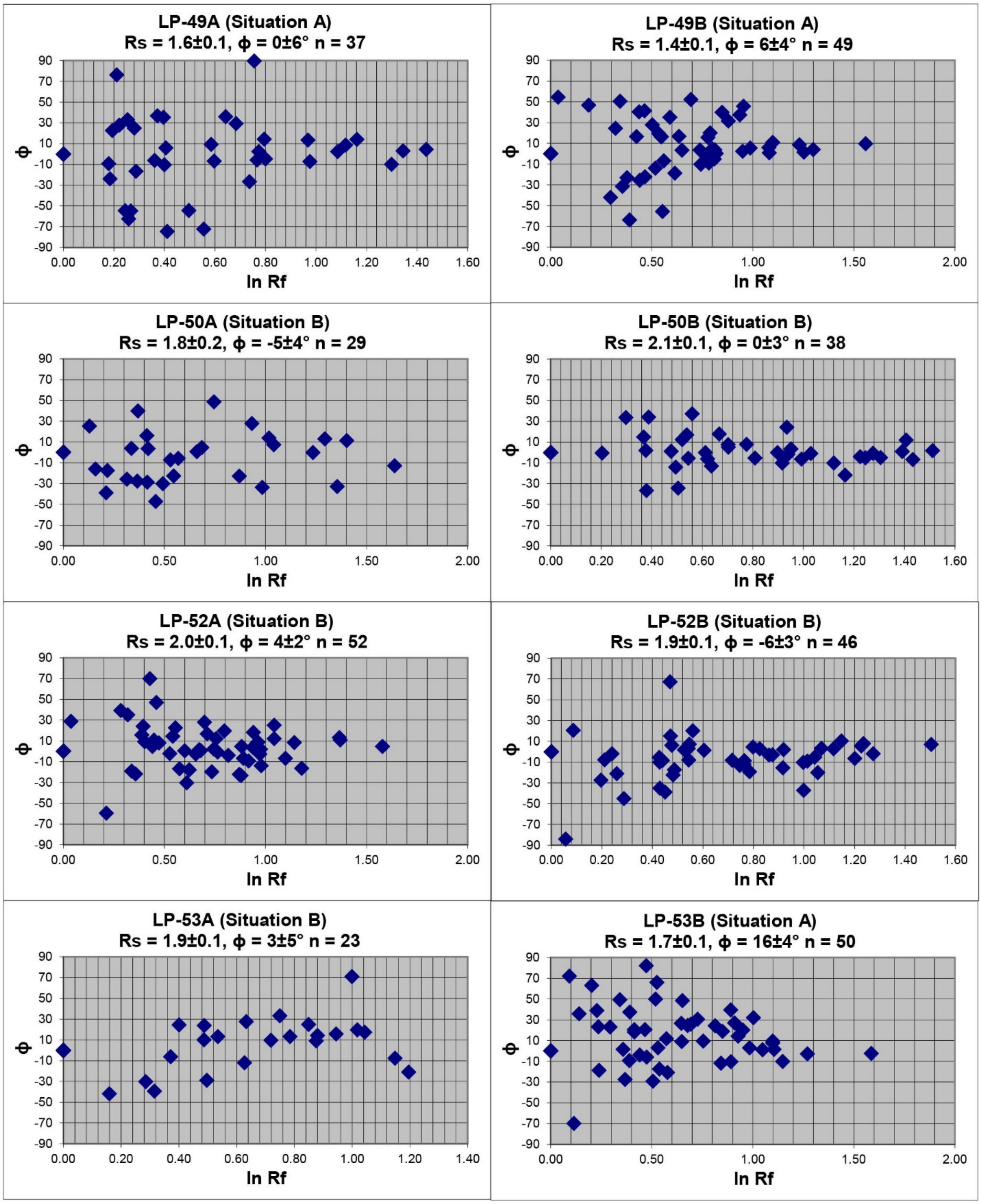

LP-49A (Situation A)
Rs = 1.6±0.1, ϕ = 0±6° n = 37
LP-49B (Situation A)
Rs = 1.4±0.1, ϕ = 6±4° n = 49
LP-50A (Situation B)
Rs = 1.8±0.2, ϕ = -5±4° n = 29
LP-50B (Situation B)
Rs = 2.1±0.1, ϕ = 0±3° n = 38
LP-52A (Situation B)
Rs = 2.0±0.1, ϕ = 4±2° n = 52
LP-52B (Situation B)
Rs = 1.9±0.1, ϕ = -6±3° n = 46
LP-53A (Situation B)
Rs = 1.9±0.1, ϕ = 3±5° n = 23
LP-53B (Situation A)
Rs = 1.7±0.1, ϕ = 16±4° n = 50
ϕ
ln Rf

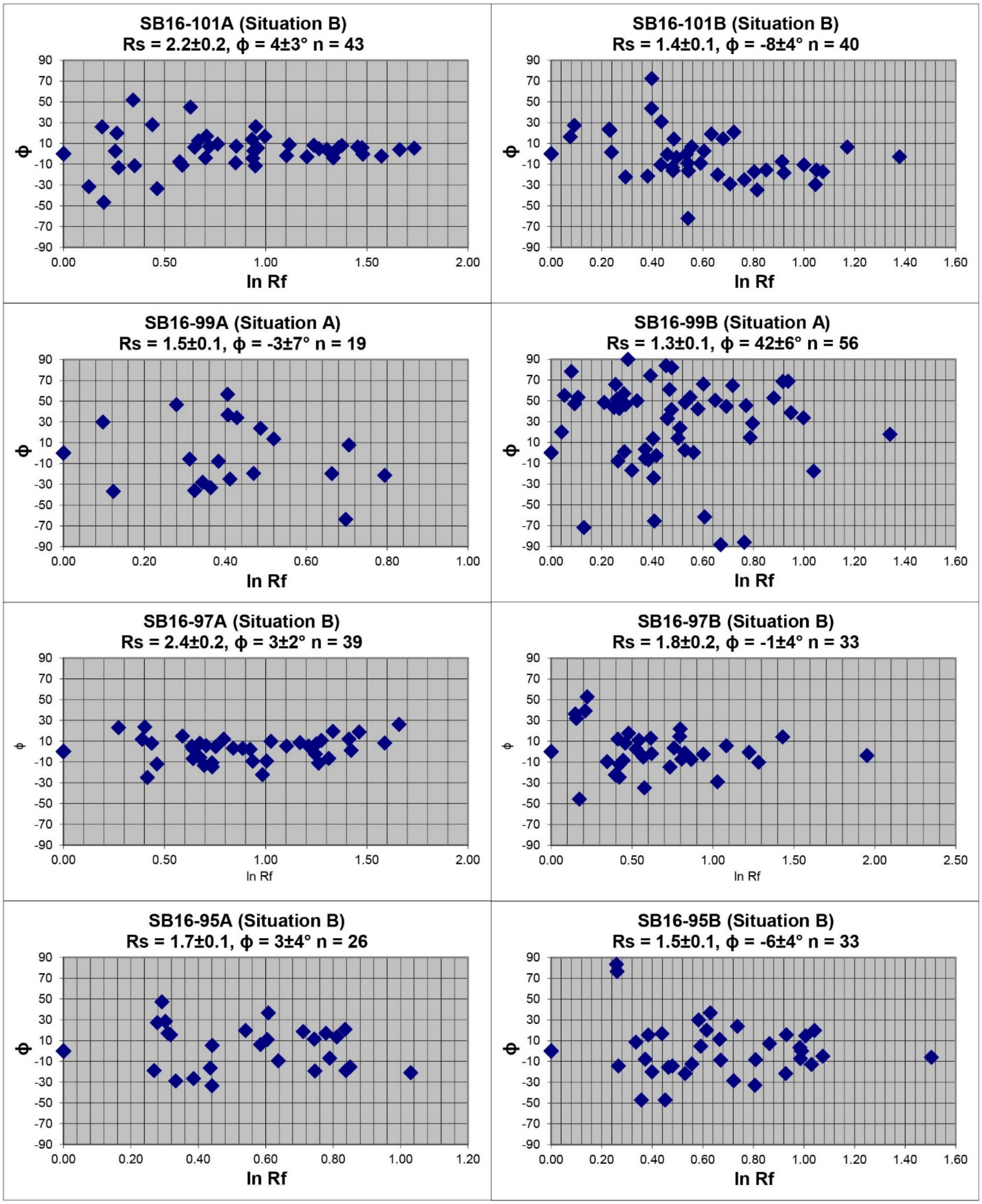
SB16-101A (Situation B)
Rs = 2.2±0.2, ϕ = 4±3° n = 43
ϕ
ln Rf
SB16-101B (Situation B)
Rs = 1.4±0.1, ϕ = -8±4° n = 40
ϕ
ln Rf
SB16-99A (Situation A)
Rs = 1.5±0.1, ϕ = -3±7° n = 19
ϕ
ln Rf
SB16-99B (Situation A)
Rs = 1.3±0.1, ϕ = 42±6° n = 56
ϕ
ln Rf
SB16-97A (Situation B)
Rs = 2.4±0.2, ϕ = 3±2° n = 39
ϕ
ln Rf
SB16-97B (Situation B)
Rs = 1.8±0.2, ϕ = -1±4° n = 33
ϕ
ln Rf
SB16-95A (Situation B)
Rs = 1.7±0.1, ϕ = 3±4° n = 26
ϕ
ln Rf
SB16-95B (Situation B)
Rs = 1.5±0.1, ϕ = -6±4° n = 33
ϕ
ln Rf

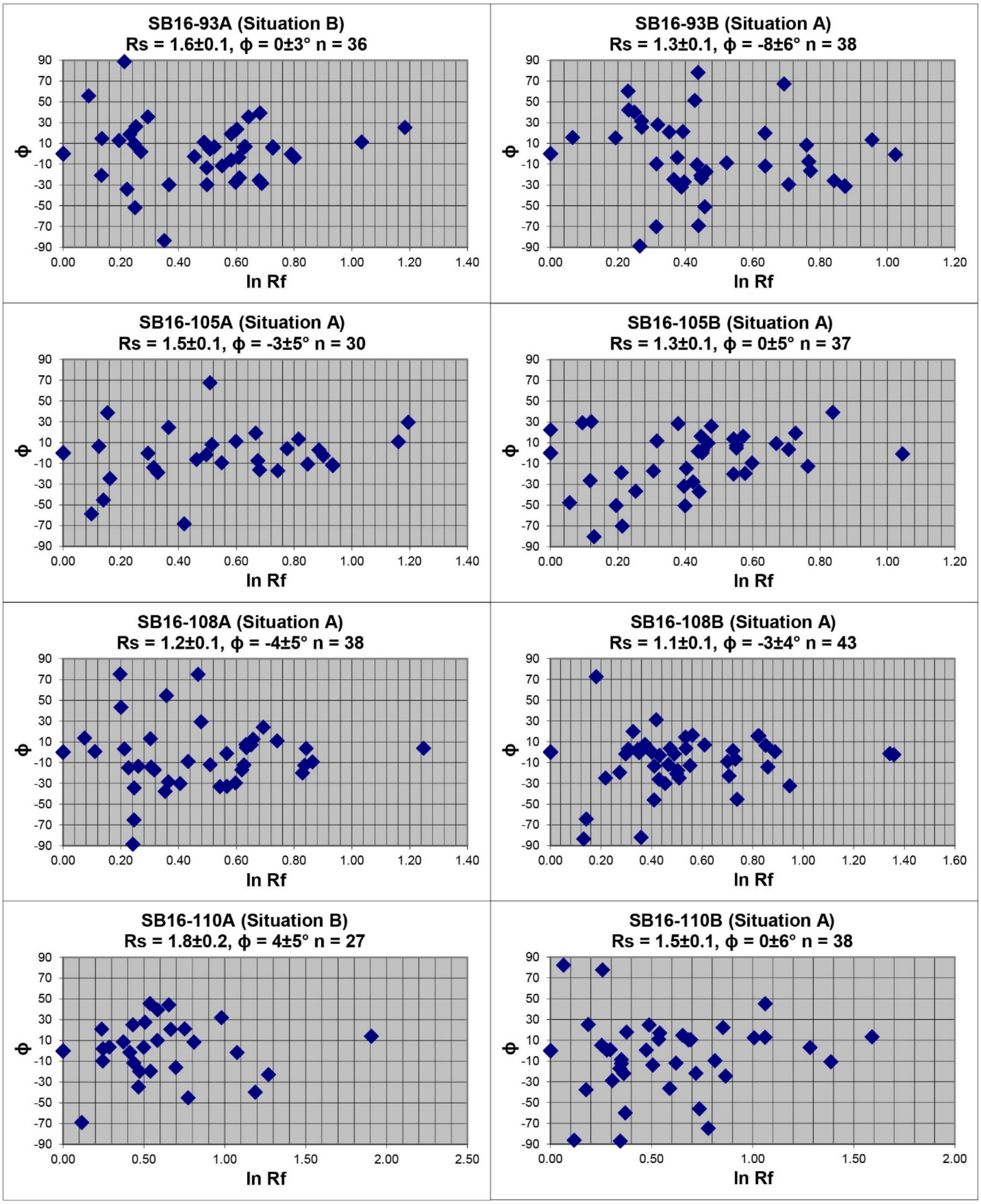
SB16-93A (Situation B)
Rs = 1.6±0.1, ϕ = 0±3° n = 36
SB16-93B (Situation A)
Rs = 1.3±0.1, ϕ = -8±6° n = 38
SB16-105A (Situation A)
Rs = 1.5±0.1, ϕ = -3±5° n = 30
SB16-105B (Situation A)
Rs = 1.3±0.1, ϕ = 0±5° n = 37
SB16-108A (Situation A)
Rs = 1.2±0.1, ϕ = -4±5° n = 38
SB16-108B (Situation A)
Rs = 1.1±0.1, ϕ = -3±4° n = 43
SB16-110A (Situation B)
Rs = 1.8±0.2, ϕ = 4±5° n = 27
SB16-110B (Situation A)
Rs = 1.5±0.1, ϕ = 0±6° n = 38
ϕ
ln Rf

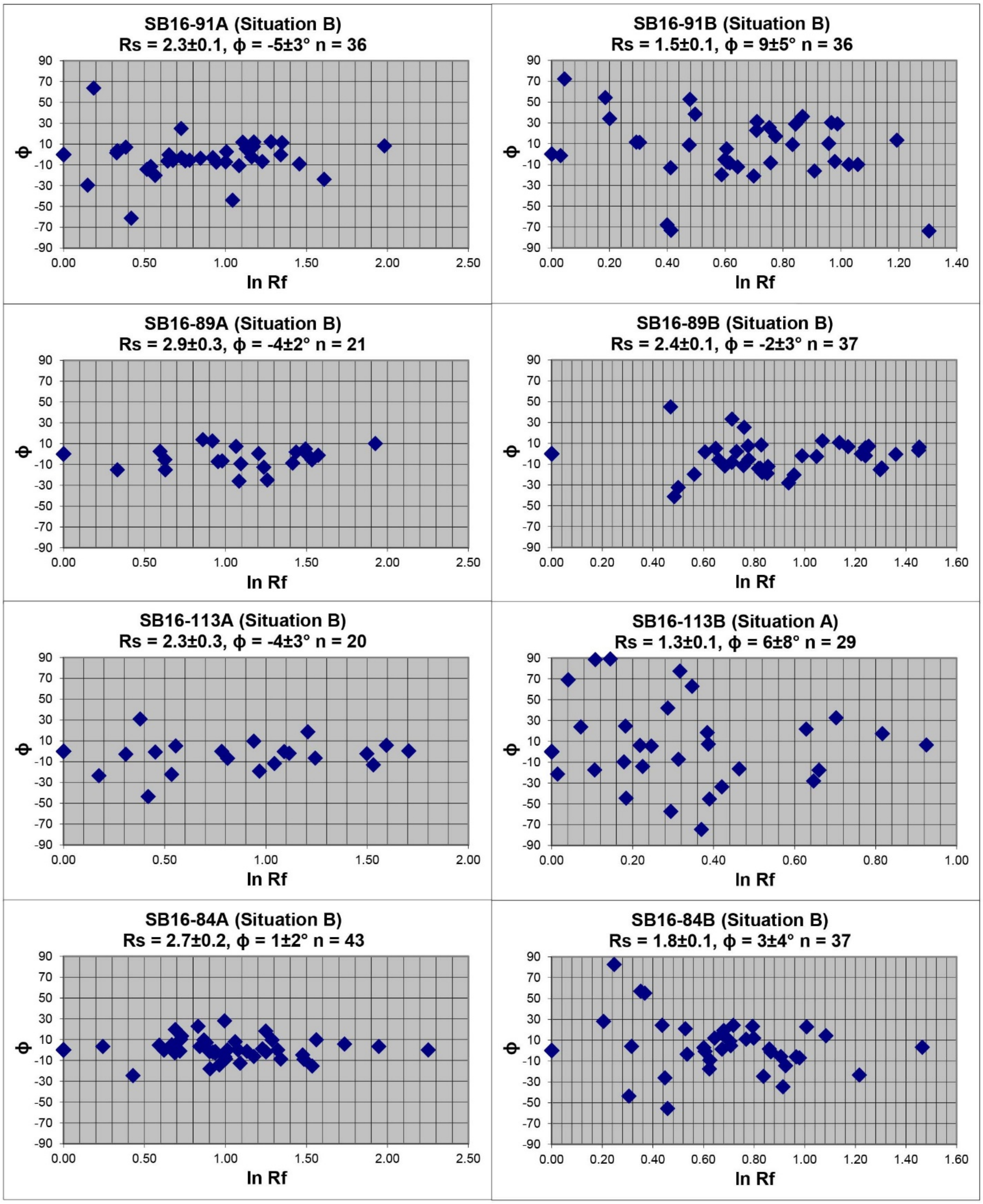
SB16-91A (Situation B)
Rs = 2.3±0.1, ϕ = -5±3° n = 36
SB16-91B (Situation B)
Rs = 1.5±0.1, ϕ = 9±5° n = 36
SB16-89A (Situation B)
Rs = 2.9±0.3, ϕ = -4±2° n = 21
SB16-89B (Situation B)
Rs = 2.4±0.1, ϕ = -2±3° n = 37
SB16-113A (Situation B)
Rs = 2.3±0.3, ϕ = -4±3° n = 20
SB16-113B (Situation A)
Rs = 1.3±0.1, ϕ = 6±8° n = 29
SB16-84A (Situation B)
Rs = 2.7±0.2, ϕ = 1±2° n = 43
SB16-84B (Situation B)
Rs = 1.8±0.1, ϕ = 3±4° n = 37
ϕ
ln Rf

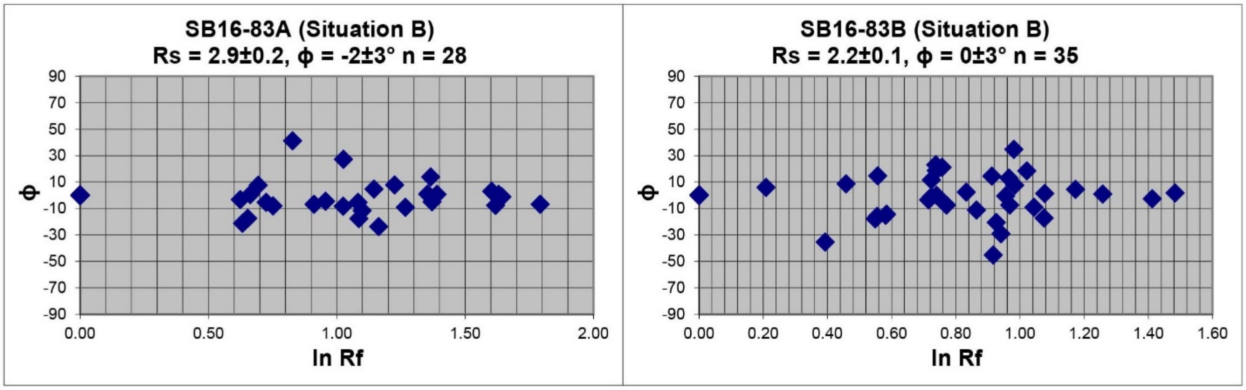

Discussion DR5: Evidence supporting assumptions for estimation of W_m using the Rs-θ' method

Assuming plane strain, and idealized, steady-state flow, the relationship between tectonic strain (Rs) and the angle between foliation and the long axis of the strain ellipsoid (θ') can be used to estimate W_m (Fossen and Tikoff, 1993; Tikoff and Fossen, 1995). W_m can be measured by plotting the Rs value of the transport-parallel ('A') thin section versus the corresponding θ' value, and comparing to graphed lines of constant W_m (e.g., Tikoff and Fossen, 1995; Yonkee, 2005). This involves assumption that the orientation of macroscopic foliation approximates the 'shear zone boundary', or boundary of the 'high strain zone' (Tikoff and Fossen, 1995). As illustrated in mapping in Bhutan and other regions of the Himalaya, 1st-order Himalayan shear zones such as the STDS are oriented subparallel to macroscopic foliation for significant across-strike map distances, including ≥50 km in the Lingshi region of northwestern Bhutan (Long et al., 2011; Kellett and Grujic, 2012; this study), ≥75 km in north-central Nepal (Robinson et al., 2006), and ≥100 km in the Himachal Himalaya in northwestern India (Webb, 2013). This justifies the assumption that macroscopic foliation is approximately parallel to the boundaries of major Himalayan shear zones such as the STDS.

Discussion DR6: Calculation of transport-parallel lengthening and transport-normal shortening.

Restoration of the 3D strain ellipsoid for each sample to a sphere allowed estimation of elongations in the X and Y directions and shortening in the Z direction (Table DR3). The Y elongation obtained from this exercise was used to calculate the corrected flow-plane parallel and flow-plane normal elongations discussed below (e.g., Law, 2010; Xypolias et al., 2010).

For calculation of flow plane-parallel (i.e., transport-parallel) lengthening and flow-plane-normal (i.e., transport-normal) shortening, the equations of Figure 10 of Law (2010), which integrate strain ratio in the X/Z plane ($Rs_{[X/Z]}$) with mean kinematic vorticity number (W_m), were utilized. Because a range of W_m values for each sample was estimated with the Rs-θ' method (due to assignment of a 1 SE range for estimation of θ' values; e.g., Long et al., 2016; 2017), the low and high ranges of W_m values were used to estimate a permissible range of lengthening and shortening values. As these values do not account for lengthening in the Y direction, they are listed in Table DR3 as 'uncorrected'.

Next, using the Y lengthening values estimated for each sample from restoration of the ellipsoid to a sphere (the 'percent stretch in Y' on the graphs of Law, 2010, his Fig. 11, and Xypolias et al., 2010, their Fig. 11), corrected values for transport-parallel lengthening and transport-normal shortening were calculated that account for lengthening in Y. These corrected values were calculated for the low and high ranges of W_m for each sample. These corrected ranges are listed on Table 4 in the text, and plotted on Figure 10E-F.

Six low-strain magnitude (Rs typically ≤ 1.3) samples from strain domain 3 (48, 46, 45, 37, 36, 34), four of which exhibit W_m values as high as ~0.65-0.85, yielded negative values for corrected transport-parallel lengthening and corrected transport-normal shortening for the high range of their W_m values. This indicates the potential for a component of lengthening normal to the transport direction and a component of shortening parallel to the transport direction. These data that yielded negative values were not able to be plotted on the Law (2010) and Xypolias et al. (2010) figures for correction of lengthening in Y. Therefore, only the positive portion of their error range is plotted on Figure 10E-F.

Table DR3 (following two pages): Supporting data for calculation of transport-parallel lengthening and transport-normal shortening values from strain samples on the Dodena-Lingshi transect. Refer to Table DR1 for a guide to abbreviated sample numbers used in the text.

Sample	Structural height above base of Chekha Fm (km)	$Rs_{[X/Z]}$	$\theta'_{[x/z]}$	$Rs_{[Y/Z]}$	$\theta'_{[y/z]}$	$Rs_{[X/y]}$	Low W_m from Rs-θ'	High W_m from Rs-θ'	Elongation values from restoration to a sphere: Undeformed sphere diameter	Lineation-parallel (X) lengthening (%)	Lineation-normal (Y) lengthening (%)	Foliation-normal (Z) shortening (%)	Uncorrected transport-normal stretch (low Wm)	Uncorrected transport-normal shortening (%) (low Wm)	Uncorrected transport-parallel stretch (low Wm)	Uncorrected transport-parallel lengthening (%) (low Wm)
LP-33	9.675	1.2	3	1.2	18	1.0	0.00	0.30	1.13	6	6	11	0.91	9	1.10	10
LP-34	9.575	1.1	4	1.1	-10	1.0	0.00	0.35	1.07	3	3	6	0.95	5	1.05	5
LP-35	9.475	1.4	-2	1.4	-8	1.0	0.00	0.25	1.25	12	12	20	0.85	15	1.18	18
LP-36	8.775	1.1	14	1.1	11	1.0	0.20	0.70	1.07	3	3	6	0.97	3	1.03	3
LP-37	8.450	1.3	19	1.1	10	1.2	0.45	0.85	1.13	15	-2	11	1.00	0	1.00	0
LP-45	5.700	1.5	-16	1.4	17	1.1	0.55	0.75	1.28	17	9	22	1.01	-1	0.99	-1
LP-46	4.950	1.2	14	1.1	-11	1.1	0.35	0.65	1.10	9	0	9	0.98	2	1.02	2
LP-48	4.700	1.1	3	1.1	17	1.0	0.00	0.35	1.07	3	3	6	0.95	5	1.05	5
LP-49	4.650	1.6	0	1.4	6	1.1	0.00	0.25	1.31	22	7	24	0.79	21	1.26	26
LP-50	4.425	2.1	0	1.8	-5	1.2	0.00	0.15	1.56	35	16	36	0.69	31	1.45	45
LP-52	3.600	2.0	4	1.9	-6	1.1	0.10	0.30	1.56	28	22	36	0.71	29	1.40	40
LP-53	3.275	1.9	3	1.7	16	1.1	0.00	0.40	1.48	29	15	32	0.73	27	1.38	38
SB16-101	2.375	2.2	4	1.4	-8	1.6	0.05	0.40	1.45	51	-4	31	0.68	32	1.48	48
SB16-99	2.225	1.5	-3	1.3	42	1.2	0.00	0.45	1.25	20	4	20	0.82	18	1.22	22
SB16-97	1.975	2.4	3	1.8	-1	1.3	0.05	0.30	1.63	47	11	39	0.65	35	1.55	55
SB16-95	1.775	1.7	3	1.5	-6	1.1	0.00	0.35	1.37	24	10	27	0.77	23	1.30	30
SB16-93	1.600	1.6	0	1.3	-8	1.2	0.00	0.25	1.28	25	2	22	0.79	21	1.26	26
SB16-105	1.275	1.5	-3	1.3	0	1.2	0.00	0.35	1.25	20	4	20	0.82	18	1.22	22
SB16-108	1.175	1.2	-4	1.1	-3	1.1	0.00	0.35	1.10	9	0	9	0.91	9	1.10	10
SB16-110	0.850	1.8	4	1.5	0	1.2	0.00	0.45	1.39	29	8	28	0.75	25	1.34	34
SB16-91	0.775	2.3	-5	1.5	9	1.5	0.10	0.45	1.51	52	-1	34	0.66	34	1.51	51
SB16-89	0.700	2.9	-4	2.4	-2	1.2	0.15	0.40	1.91	52	26	48	0.60	40	1.67	67
SB16-113	0.450	2.3	-4	1.3	6	1.8	0.05	0.40	1.44	60	-10	31	0.66	34	1.51	51
SB16-84	0.250	2.7	1	1.8	3	1.5	0.00	0.20	1.69	59	6	41	0.61	39	1.64	64
SB16-83	0.175	2.9	-2	2.2	0	1.3	0.00	0.35	1.85	56	19	46	0.59	41	1.70	70

Corrected transport-parallel lengthening (%) (low Wm)	Uncorrected transport-normal stretch (high Wm)	Uncorrected transport-normal shortening (%) (high Wm)	Uncorrected transport-parallel stretch (high Wm)	Uncorrected transport-parallel lengthening (%) (high Wm)	Corrected transport-parallel lengthening (%) (high Wm)	Corrected transport-parallel lengthening (%) (middle of range)	Corrected transport-parallel lengthening (%) (error range)	Corrected transport-normal shortening (%) (middle of range)	Corrected transport-normal shortening (%) (error range)
4	0.96	4	1.04	4	2	3.0	1.0	6.3	2.4
2	1.02	-2	0.98	-2	0	1.0	1.0	1.3	3.4
8	0.88	12	1.14	14	5	6.5	1.5	13.9	1.6
2	1.35	-35	0.74	-26	0	1.0	1.0	1.3	1.3
0	1.77	-77	0.56	-44	0	0.0	0.0	0.2	0.2
0	1.32	-32	0.76	-24	0	0.0	0.0	0.0	0.0
2	1.23	-23	0.81	-19	0	1.0	1.0	1.0	1.0
2	1.02	-2	0.98	-2	0	1.0	1.0	1.3	3.4
18	0.82	18	1.22	22	14	16.0	2.0	19.3	1.6
25	0.70	30	1.43	43	24	24.5	0.5	30.5	0.5
18	0.75	25	1.33	33	15	16.5	1.5	26.8	2.0
22	0.81	19	1.23	23	10	16.0	6.0	23.1	4.3
55	0.76	24	1.32	32	39	47.0	8.0	28.3	4.2
17	0.93	7	1.07	7	3	10.0	7.0	12.5	5.9
38	0.69	31	1.45	45	30	34.0	4.0	33.2	2.2
18	0.83	17	1.20	20	10	14.0	4.0	20.0	3.3
24	0.82	18	1.22	22	19	21.5	2.5	19.3	1.6
17	0.88	12	1.13	13	8	12.5	4.5	15.0	3.3
10	0.98	2	1.02	2	2	6.0	4.0	5.3	3.4
23	0.86	14	1.16	16	8	15.5	7.5	19.7	5.8
54	0.77	23	1.30	30	32	43.0	11.0	28.3	5.3
34	0.67	33	1.50	50	22	28.0	6.0	36.8	3.5
70	0.74	26	1.34	34	52	61.0	9.0	29.8	4.2
56	0.63	37	1.60	60	51	53.5	2.5	38.2	0.9
43	0.65	35	1.55	55	30	36.5	6.5	38.3	3.0

Figure DR6: Ternary plot showing point (P), girdle (G), and random (R) values for quartz petrofabric samples from the Lingshi transect. Samples were plotted using methods described in Vollmer (1990) and are shown with intensity contours defined by Lisle (1985). See Figure 9D in the text for a graph of cylindricity (B) values relative to structural height.

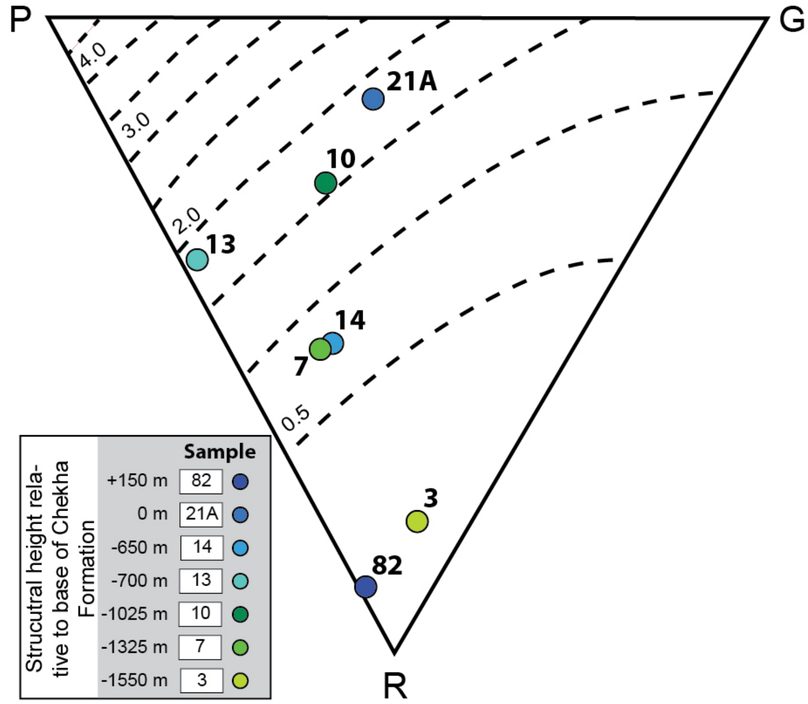

Figure DR7: Graph of average recrystallized quartz grain diameter versus structural height for the seven samples on which quartz petrofabric data were collected. Error is shown at the 1σ level, and 'n' represents the number of grains measured. Numbers in bold indicate sample numbers. Grain sizes were measured by tracing the outlines of >100 adjacent grains in Adobe Illustrator, and then using the 'ellipse fit' function in ImageJ (Schneider et al., 2012). The long and short axes of each ellipse were then converted into the diameter of a circle with an equivalent area.

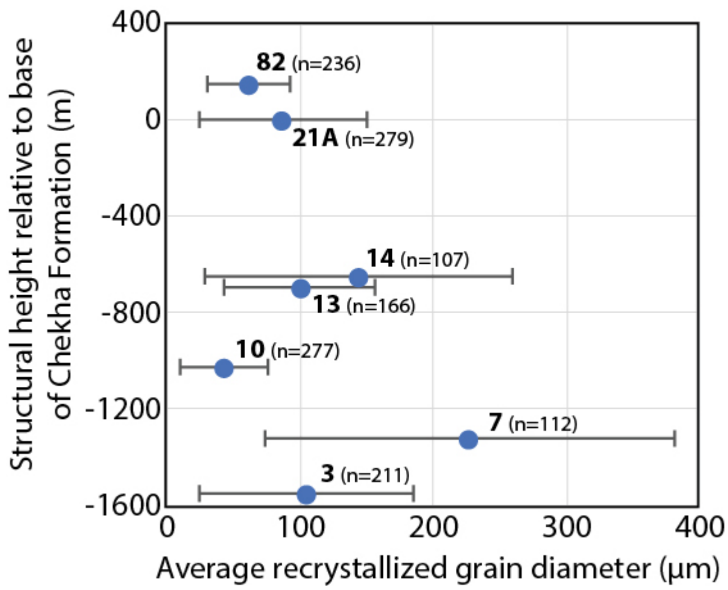

REFERENCES CITED

Beyssac, O., Goffe, B., Petitet, J.P., Froigneux, E., Moreau, M., and Rouzaud, J.N., 2003, On the characterization of disordered and heterogeneous carbonaceous materials by Raman spectroscopy: Spectrochimica Acta Part A, v. 59, p. 2267–2276, https://doi.org/10.1016/S1386-1425(03)00070-2.

Cooper, F.J., Hodges, K.V., and Adams, B.A., 2013, Metamorphic constraints on the character and displacement of the South Tibetan fault system, central Bhutanese Himalaya: Lithosphere, v. 5, p. 67–81, https://doi.org/10.1130/L221.1.

Dunnet, D., 1969, A technique for finite strain analysis using elliptical particles: Tectonophysics, v. 7, p. 117–136, https://doi.org/10.1016/0040-1951(69)90002-X.

Faleiros, F.M., Moraes, R., Pavan, M., and Campanha, G.A.C., 2016, A new empirical calibration of the quartz c-axis fabric opening-angle deformation thermometer: Tectonophysics, v. 671, p. 173–182, https://doi.org/10.1016/j.tecto.2016.01.014.

Fossen, H., and Tikoff, B., 1993, The deformation matrix for simultaneous simple shearing, pure shearing and volume change, and its application to transpression–transtension tectonics:

Journal of Structural Geology, v. 15, p. 413–422, https://doi.org/10.1016/0191-8141(93)90137-Y.
Hunter, N.J.R., Luzin, V., and Wilson, C.J.L., 2017, Direct measurement of the quartz *c*-axis using neutron diffraction: Tectonophysics, v. 712–713, p. 464–468, https://doi.org/10.1016/j.tecto.2017.05.019.
Johnson, S.E., Lenferink, H.J., Price, N.A., Marsh, J.H., Koons, P.O., West, D.P., Jr., and Beane, R., 2009, Clast-based kinematic vorticity gauges: The effects of slip at matrix/clast interfaces: Journal of Structural Geology, v. 31, p. 1322–1339, https://doi.org/10.1016/j.jsg.2009.07.008.
Kellett, D.A., and Grujic, D., 2012, New insight into the South Tibetan detachment system: Not a single progressive deformation: Tectonics, v. 31, TC2007, https://doi.org/10.1029/2011TC002957.
Kruhl, J.H., 1998, Prism- and basal-plane parallel subgrain boundaries in quartz: A microstructural geothermobarometer [Reply]: Journal of Metamorphic Geology, v. 16, p. 142–146.
Law, R.D., 2010, Moine thrust zone mylonites at the Stack of Glencoul: II - results of vorticity analyses and their tectonic significance, in Continental Tectonics and Mountain Building - The Legacy of Peach and Horne, edited by R.D. Law, R.W.H. Butler, R. Holdsworth, M. Krabbendam, and R.A. Strachan, Geological Society of London Special Publication, v. 335, p. 579–602, doi: https://doi.org/10.1144/SP335.24.
Law, R.D., 2014, Deformation thermometry based on quartz c-axis fabrics and recrystallization microstructures: A review: Journal of Structural Geology, v. 66, p. 129–161, https://doi.org/10.1016/j.jsg.2014.05.023.
Law, R.D., Stahr, D.W., Francsis, M.K., Ashley, K.T., Grasemann, B., and Ahmad, T., 2013, Deformation temperatures and flow vorticities near the base of the Greater Himalayan Series, Sutlej Valley and Shimla Klippe, NW India: Journal of Structural Geology, v. 54, p. 21–53, https://doi.org/10.1016/j.jsg.2013.05.009.
Lisle, R.J., 1977, Estimation of the tectonic strain ratio from the mean shape of deformed elliptical markers: Geologie & Mijnbouw, v. 56, p. 140–144.
Lisle, R.J., 1979, Strain analysis using deformed pebbles: the influence of initial pebble shape: Tectonophysics, v. 60, p. 263–277, https://doi.org/10.1016/0040-1951(79)90163-X.
Lisle, R.J., 1985, The use of the orientation tensor for the description and statistical testing of fabrics: Journal of Structural Geology, v. 7, p. 115–117, https://doi.org/10.1016/0191-8141(85)90119-1.
Lister, G.S., Paterson, M.S., and Hobbs, B.E., 1978, The simulation of fabric development in plastic deformation and its application to quartzite: The model: Tectonophysics, v. 45, p. 107–158, https://doi.org/10.1016/0040-1951(78)90004-5.
Lister, G.S., and Williams, P.F., 1979, Fabric development in shear zones: theoretical controls and observed phenomena: Journal of Structural Geology, v. 1, p. 283–297, https://doi.org/10.1016/0191-8141(79)90003-8.
Lister, G.S., and Hobbs, B.E., 1980, The simulation of fabric development during plastic deformation and its application to quartzite: the influence of deformation history: Journal of Structural Geology, v. 2, p. 355–370, https://doi.org/10.1016/0191-8141(80)90023-1.
Long, S.P., McQuarrie, N., Tobgay, T., Grujic, D., and Hollister, L., 2011, Geologic map of Bhutan: The Journal of Maps, v2011, p. 184–192, 1:500,000-scale, doi:10.4113/jom.2011.1159.

Long, S.P., Gordon, S.M., Young, J.P., and Soignard, E., 2016, Temperature and strain gradients through Lesser Himalayan rocks and across the Main Central thrust, south-central Bhutan: implications for transport-parallel stretching and inverted metamorphism: Tectonics, v. 35, https://doi.org/10.1002/2016TC004242.

Long, S.P., Gordon, S.M., and Soignard, E., 2017, Distributed north-vergent shear and flattening through Greater and Tethyan Himalayan rocks: insights from metamorphic and strain data from the Dang Chu region, central Bhutan: Lithosphere, v. 9, p. 774–795, https://doi.org/10.1130/L655.1.

Morgan, S., and Law, R.D., 2004, Unusual transition in quartzite dislocation creep regimes and crystal slip systems in the aureole of the Eureka Valley-Joshua Flat-Beer Creek pluton, California: A case for anhydrous conditions created by decarbonation reactions: Tectonophysics, v. 384, p. 209–231, https://doi.org/10.1016/j.tecto.2004.03.016.

Passchier, C.W., and Trouw, R.A.J., 2005, Micro-tectonics, 2nd edition, Springer, New York, 366 p.

Peternell, M., Hasalová, P., Wilson, C.J.L., Piazolo, S., and Schulmann, K., 2010, Evaluating quartz crystallographic preferred orientations and the role of deformation partitioning using EBSD and fabric analyser techniques: Journal of Structural Geology, v. 32, p. 803–817, https://doi.org/10.1016/j.jsg.2010.05.007.

Rahl, J.M., Anderson, K.M., Brandon, M.T., and Fassoulas, C., 2005, Raman spectroscopic carbonaceous material thermometry of low-grade metamorphic rocks: Calibration and application to tectonic exhumation in Crete, Greece: Earth and Planetary Science Letters, v. 240, p. 339–354, https://doi.org/10.1016/j.epsl.2005.09.055.

Ramsay, J.G., 1967, Folding and fracturing of rocks: McGraw-Hill, New York, 560 p.

Ramsay, J.G., and Huber, M.I., 1983, Techniques of Modern Structural Geology, Vol. 1: Strain Analysis: Academic Press, London, 307 p.

Robinson, D.M., DeCelles, P.G., and Copeland, P., 2006, Tectonic evolution of the Himalayan thrust belt in western Nepal: implications for channel flow models: Geological Society of America Bulletin, v. 118, p. 865–885, https://doi.org/10.1130/B25911.1.

Sander, B., 1950, Einführung in die Gefügekunde der Geologischen Körper, Zweiter Teil, Die Korngefuege: Springer-Verlag, Wein-Inssbruck, 412 p, https://doi.org/10.1007/978-3-7091-7759-4.

Schneider, C.A., Rasband, W.S., and Eliceiri, K.W., 2012, NIH Image to ImageJ: 25 years of image analysis: Nature Methods, v. 9, p. 671–675, https://doi.org/10.1038/nmeth.2089.

Tikoff, B., and Fossen, H., 1995, The limitations of three-dimensional kinematic vorticity analysis: Journal of Structural Geology, v. 17, p. 1771–1784, https://doi.org/10.1016/0191-8141(95)00069-P.

Vollmer, F.W., 1990, An application of eigenvalue methods to structural domain analysis: Geological Society of America Bulletin, v. 102, p. 786–791, https://doi.org/10.1130/0016-7606(1990)102<0786:AAOEMT>2.3.CO;2.

Vollmer, F.W., 2017, [Spherical projection and orientation data analysis program. www.frederickvollmer.com]: Orient (Paris), v. 3, p. •••.

Wallis, S.R., 1992, Vorticity analysis in a metachert from the Sanbagawa Belt, SW Japan: Journal of Structural Geology, v. 14, p. 271–280, https://doi.org/10.1016/0191-8141(92)90085-B.

Wallis, S.R., 1995, Vorticity analysis and recognition of ductile extension in the Sanbagawa belt, SW Japan: Journal of Structural Geology, v. 17, p. 1077–1093, https://doi.org/10.1016/0191-8141(95)00005-X.

Webb, A.A.G., 2013, Preliminary balanced palinspastic reconstruction of Cenozoic deformation across the Himachal Himalaya (northwestern India): Geosphere, v. 9, p. 572–587, https://doi.org/10.1130/GES00787.1.

Whitney, D.L., and Evans, B.W., 2010, Abbreviations for names of rock-forming minerals: The American Mineralogist, v. 95, p. 185–187, https://doi.org/10.2138/am.2010.3371.

Wilson, C.J.L., Russell-Head, D.S., Kunze, K., and Viola, G., 2007, The analysis of quartz *c*-axis fabrics using a modified optical microscope: Journal of Microscopy, v. 227, p. 30–41, https://doi.org/10.1111/j.1365-2818.2007.01784.x.

Xypolias, P., Spanos, D., Chatzaras, V., Kokkalas, S., and Koukouvelas, I., 2010, Vorticity of flow in ductile thrust zones: examples from the Attico-Cycladic Massif (Internal Hellenides, Greece): in Continental Tectonics and Mountain Building - The Legacy of Peach and Horne, edited by R.D. Law, R.W.H. Butler, R. Holdsworth, M. Krabbendam, and R.A. Strachan, Geological Society of London Special Publication, v. 335, p. 687–714, doi: https://doi.org/10.1144/SP335.28.

Yonkee, A., 2005, Strain patterns within part of the Willard thrust sheet, Idaho-Wyoming-Utah thrust belt: Journal of Structural Geology, v. 27, p. 1315–1343, https://doi.org/10.1016/j.jsg.2004.06.014.